Mon. Not. R. Astron. Soc. **386,** 1709–1728 (2008) doi:10.1111/j.1365-2966.2008.13162.x

An *XMM–Newton* study of the environments, particle content and impact of low-power radio galaxies

J. H. Croston,[1]★ M. J. Hardcastle,[1] M. Birkinshaw,[2] D. M. Worrall[2] and R. A. Laing[3]

[1] *School of Physics, Astronomy and Mathematics, University of Hertfordshire, College Lane, Hatfield, Hertfordshire AL10 9AB*
[2] *H. H. Wills Physics Laboratory, University of Bristol, Tyndall Avenue, Bristol BS8 1TL*
[3] *European Southern Observatory, Karl-Schwarzschild-Straße 2, D-85748 Garching-bei-München, Germany*

Accepted 2008 February 25. Received 2008 February 22; in original form 2008 January 15

ABSTRACT

We present a detailed study of the environments of a sample of nine low-power [Fanaroff–Riley type I (FR I)] radio galaxies, based on new and archival *XMM–Newton* observations. We report new detections of group-scale environments around three radio galaxies: 3C 296, NGC 1044 and 3C 76.1. As with previous studies, we find that FR I radio galaxies inhabit group environments ranging over nearly two orders of magnitude in bolometric X-ray luminosity; however, we find no evidence for a tight relationship between large-scale X-ray environment and radio-source properties such as size, radio luminosity and axial ratio. This leads us to conclude that radio-source evolution cannot be determined entirely by the global properties of the hot gas. We confirm earlier work showing that equipartition internal pressures are typically lower than the external pressures acting on the radio lobes, so that additional non-radiating particles must be present. We present the first direct observational evidence that entrainment may provide this missing pressure, in the form of a relationship between radio-source structure and apparent pressure imbalance. Finally, our study provides further support for the presence of an apparent temperature excess in radio-loud groups compared to the group population as a whole. For five of eight temperature excesses, the energy required to inflate the radio lobes is comparable to the energy required to produce this excess by heating of the group gas; however, in three cases the current radio source appears too weak to produce the temperature excess. It remains unclear whether the temperature excess can be directly associated with the current phase of active galactic nuclei (AGN) activity, or whether it is instead either a signature of previous AGN activity or simply an indicator of the particular set of group properties most conducive to the growth of an FR I radio galaxy.

Key words: galaxies: active – X-rays: galaxies: clusters.

1 INTRODUCTION

The dynamics of low power [Fanaroff–Riley type I (FR I): Fanaroff & Riley 1974], twin-jet radio galaxies are thought to be controlled by interactions between the initially highly relativistic jets and the surrounding hot-gas medium, which act to decelerate the jets significantly on scales of typically a few kpc (e.g. Bicknell 1994; Laing & Bridle 2002a). On scales of hundreds of kpc, low-power radio galaxies exhibit a wide range of morphologies, from narrowly collimated plumes to large, rounded lobes (e.g. Laing 1993). In order to understand how such structures are produced, and to investigate the evolution of FR I sources on large scales, it is necessary to have good constraints on the hot-gas environments that confine their radio lobes. *ROSAT* observations first established that the brightest and most well-studied FR I radio galaxies usually reside in group-scale environments (e.g. Worrall & Birkinshaw 1994; Komossa & Böhringer 1999; Worrall & Birkinshaw 2000). With *Chandra* and *XMM–Newton*, it is possible to study radio-galaxy environments and jet/environment interactions in more detail (e.g. Blanton et al. 2001; Croston et al. 2003; Fabian et al. 2003); however, while there have been many studies of the apparent impact of FR I sources in clusters, to date there have been few detailed *Chandra* and *XMM–Newton* studies of the environmental properties of nearby, well-studied FR I radio galaxies. The role of environmental properties such as group/cluster richness, gas density and temperature distribution in determining large-scale radio structure therefore remains uncertain.

Another key uncertainty both in modelling radio-galaxy dynamics and in establishing their energetic impact is the lack of constraints on particle content in FR I radio jets and lobes. In the case of powerful (FR II) radio galaxies, two lines of evidence

---

★Email: j.h.croston@herts.ac.uk

suggest that synchrotron minimum-energy estimates are roughly valid in the lobes: (i) for cases where external pressure measurements are available, they are in reasonable agreement with the internal minimum pressure (e.g. Hardcastle et al. 2002; Belsole et al. 2004; Croston et al. 2004); (ii) measurements of inverse-Compton emission from the lobes of FR II radio galaxies suggest that their electron energy densities are close to the value for equipartition with the magnetic field in the absence of an energetically important proton population (e.g. Croston et al. 2005b; Kataoka & Stawarz 2005). However, in low-power (FR I) radio galaxies, it has been known for several decades that a relativistic-electron population in equipartition with the magnetic field cannot provide sufficient pressure to balance that of the external medium (e.g. Morganti et al. 1988; Hardcastle, Worrall & Birkinshaw 1998b; Worrall & Birkinshaw 2000). In Croston et al. (2003), we showed for two FR Is that the additional pressure cannot be due solely to relativistic-electron dominance, as this would result in detectable X-ray inverse-Compton emission, which is not seen, while the presence of sufficient thermal gas at the temperature of the environment was also ruled out by the presence of deficits in X-ray surface brightness at the positions of radio lobes. This is also the case for the sample of cluster-centre FR I radio sources recently studied by Dunn, Fabian & Taylor (2005). Relativistic protons intrinsic to the jets would require extremely large ratios of proton to electron energy in order to provide the missing pressure – such high ratios are implausible as they would lead to overpressured jets on kpc scales. The most plausible origin of the required additional pressure is either material that has been entrained and heated, or magnetic dominance of the lobes; however, these scenarios are both difficult to test.

Despite these uncertainties about radio-source energetics, our understanding of the impact of radio galaxies on their environments has improved dramatically over the past few years. Direct evidence for heating by FR I radio galaxies has been found in a number of individual systems (e.g. Kraft et al. 2003; Croston, Kraft & Hardcastle 2007; Forman et al. 2007), and statistical studies have shown that radio-source heating may have a significant impact in the outer regions of galaxy groups (Croston, Hardcastle & Birkinshaw 2005a; Jetha et al. 2007). Progress in hydrodynamical modelling has shown that a range of heating mechanisms may be capable of heating the central regions of clusters to prevent cooling flows (e.g. Brüggen & Kaiser 2001; Reynolds, Heinz & Begelman 2002; Basson & Alexander 2003) and semi-analytical galaxy formation models that take into account radio-source heating appear to be able to reproduce the properties of the nearby galaxy population more accurately than has previously been possible (Bower et al. 2006; Croton et al. 2006). The growing acceptance that AGN, and particularly low-power (FR I) radio galaxies, play an essential role in galaxy and structure evolution means that it is crucial to understand which types of radio structures form under what environmental conditions, and how the environmental impact of these different structures varies.

In this paper, we present new *XMM–Newton* observations of a sample of low-power (FR I) radio galaxies, which range in morphology from tailed or plumed sources to those with lobes or bridges. We then combine this sample with previous observations and archive data to investigate the environmental properties of the nearby FR I radio-galaxy population, to constrain their particle content and dynamics and to study their environmental impact.

Throughout the paper, we use a cosmology in which $H_0 = 70\ \mathrm{km\,s^{-1}\,Mpc^{-1}}$, $\Omega_\mathrm{m} = 0.3$ and $\Omega_\Lambda = 0.7$. Spectral indices α are defined in the sense $S_\nu \propto \nu^{-\alpha}$. Errors quoted on parameters derived from model fitting correspond to the 1σ (68 per cent) confidence range for one parameter of interest, except where otherwise stated.

2 DATA ANALYSIS

We carried out *XMM–Newton* observations of a sample of five low-power (FR I) radio galaxies, 3C 296, 3C,76.1, NGC 1044, 3C 31 and NGC 315 to follow up our earlier studies of 3C 66B, 3C 449 and NGC 6251 (Croston et al. 2003; Evans et al. 2005). In this section, we describe the data analysis for the five new observations, plus one archive observation of NGC 4261 [the AGN emission detected in this observation has been described by Gliozzi, Sambruna & Brandt (2003) and Sambruna et al. (2003), and the extended emission was discussed briefly in Croston et al. (2005a)]. In Section 5, we combine these results with our previous analysis of 3C 66B, 3C 449 and NGC 6251 (Croston et al. 2003; Evans et al. 2005). Table 1 lists the observational details for the nine *XMM–Newton* observations discussed in this paper. For three of the radio galaxies, 3C 296, NGC 315 and NGC 6251, we also made use of previously published *Chandra* radial surface-brightness profiles to improve our constraints on the inner gas distributions. Details of these profiles are given in Section 3.

2.1 Radio data

All of the radio galaxies in our sample apart from NGC 1044 are well studied in the radio, with maps in the literature at multiple frequencies. Table 2 lists the radio maps used in the figures and analysis that follows.

Table 1. Details of the new, archival and previously published *XMM–Newton* observations discussed in this paper.

Object	z	Angle scale (kpc/arcsec)	N_H (10^{20} cm^{-2})	Observations ID	Date	Exposure MOS1, MOS1, pn (s)
NGC 315	0.016	0.326	5.88	0305 290 201	2005-07-02	15 236, 14 984, 12 580
3C 31	0.017	0.346	5.39	0305 290 101	2005-08-03	14 734, 14 745, 10 819
3C 66B	0.0215	0.435	8.36	0002 970 201	2002-02-05	17 915, 17 862, 14 692[1]
NGC 1044	0.021	0.425	8.76	0201 860 301	2004-07-18	13 674, 13 839, 13 565
3C 76.1	0.032	0.639	10.8	0201 860 201	2004-08-02	17 762, 18 165, 10 961
NGC 4261	0.0073	0.150	1.55	0056 340 101	2001-12-16	26 150, 26 191, 16 257
3C 296	0.024	0.484	1.86	0201 860 101	2004-08-05	19 584, 20 315, 14 729
NGC 6251	0.0244	0.492	5.58	0056 340 201	2002-03-26	23 725, 24 715, 8074[1]
3C 449	0.0171	0.348	11.8	0002 970 101	2001-12-09	20 865, 20 837, 16 708[1]

[1] The exposure times quoted for the three previously published data sets are lifetimes after GTI-filtering using hardband light curves, similar to the method used for the new observations, as described in Croston et al. (2003) and Evans et al. (2005).

Table 2. Details of the new and previously published radio maps used in the analysis presented in this paper. The radio map for NGC 4261 was made from archival VLA data. (WSRT = Westerbork Synthesis Radio Telescope.)

Object	Frequency (GHz)	Observatory	Date observed	Reference/Proposal ID
NGC 315	1.365	VLA	2001 March 10	Laing et al. (2006)
3C 31	1.636	VLA	1995 April 28	Laing et al. (2008)
3C 66B	1.425	VLA	1994 November 10	Hardcastle et al. (1996)
NGC 1044	1.425	VLA	2004 March 19	AC712, AH276
3C 76.1	1.477	VLA	1987 November 25	Leahy et al. (1998)
NGC 4261	1.550	VLA	1984 April 23	AP77
3C 296	1.452	VLA	1987 November 25	Leahy et al. (1998)
NGC 6251	0.337	WSRT	1988 May 12	Leahy et al. (1998)
3C 449	0.609	WSRT	–	Leahy et al. (1998)

As existing low-frequency Very Large Array (VLA) observations of NGC 1044 did not fully sample its large-scale structure, we observed it with the VLA at 20 cm to supplement existing archival data. In combination with these archival data, the new observations were used to produce a good-quality map of the large-scale radio structure for comparison with X-ray images. The VLA observations were carried out on 2004 March 19 in C configuration and 2004 July 17 in D configuration. The new data, together with an short archival observation in the C configuration (AH276), were externally calibrated in the standard manner using AIPS. Each data set was then imaged, cleaned and self-calibrated individually. The two C-configuration data sets were combined and imaged after first self-calibrating the archive data set using a model from the new observations. The D-configuration data were then self-calibrated using the combined C-configuration model. Finally, the C- and D-configuration data were combined with appropriate weights and used to produce the images shown below.

2.2 *XMM–Newton* data

The data for the five new observations and one archival data set not previously analysed were reprocessed using the *XMM–Newton* SAS version 6.0.0, and the latest calibration files from the *XMM–Newton* website. The pn data were filtered to include only single and double events (PATTERN $\leqslant 4$), and FLAG = 0, and the MOS data were filtered according to the standard flag and pattern masks (PATTERN $\leqslant$ 12 and #XMMEA_EM, excluding bad columns and rows).

Several of the data sets were badly affected by background flares, and so good time-interval (GTI) filtering was applied in order to ensure that accurate measurements could be made in low surface-brightness regions. Filtering was carried out by applying a ±20 per cent clip to a light curve in the energy range where the effective area for X-rays is negligible (10–12 keV for MOS, 12–14 keV for pn). In one case, NGC 315, initial analysis revealed significant contamination from soft proton flares, and so for this source a second stage of filtering was applied using the full energy range of 0.3–10 keV and an off-source region, so as to remove any additional soft flares, again by applying a ±20 per cent cut.

To enable the use of double background-subtraction techniques for spectral and spatial analysis (see Section 2.3), the event lists were vignetting corrected using the SAS task *evigweight*. Filter-wheel closed data sets (Pointecouteau et al., private communication) for particle background subtraction were processed and filtered in the same way as the source data sets: the event lists for each camera were first filtered using the same FLAG and PATTERN filters as the data files, and weighted using *evigweight*. Weighting the particle background events lists allows this background component to be subtracted correctly from the particle component in the source files, which must be weighted up in order that the vignetting correction is applied correctly to the source and background X-ray emission in the target observation. Appropriate background files were then generated for each source using *attcalc* to recast the events list to the correct physical coordinates. The resulting background file appropriate to each source events file was used as part of the double-subtraction process in the analysis described below. A scaling factor was determined for each background data set to account for differences in the normalization of the particle and instrumental background between the source and filter-wheel closed data sets. The scaling factors were calculated by comparing the 10–12 keV (MOS) or 12–14 keV (pn) count rates for the source and background data sets. The background data products were scaled by this factor before carrying out background subtraction of spectra or profiles.

In the case of the pn camera, it is also necessary to take into account the contribution of out-of-time events: 6.3 per cent of detected pn counts (in full-frame mode) are recorded with an incorrect detector coordinate in the y direction. These events produce an additional position-dependent background component that can be important in the analysis of low surface-brightness emission. We therefore generated an out-of-time events list for the pn camera using *epchain*, which was scaled appropriately and subtracted as an additional background component in the analysis that follows.

2.3 X-ray analysis

2.3.1 *Imaging and spectral analysis*

In order to make pictures of the extended emission and to make overlays on the radio emission, we extracted images in the 0.5–5 keV energy range from the three EPIC cameras for each data set using *evselect* (these images were not used in our quantitative analysis). We then combined the images to produce a single image for each source, weighting the two MOS images by a factor chosen to increase the MOS sensitivity to be equivalent to that of the pn data (this is necessary in order to remove chip-gap artefacts from the image). The combined image was then exposure corrected using an exposure map made by summing appropriate maps for each camera obtained using *eexpmap*. This method is similar to that used by Böhringer et al. (2007). The images were not corrected for vignetting as this excessively weights up the unvignetted particle background at large radii. Point sources were then identified and removed from the combined image, and Gaussian smoothing was applied with a range of kernel sizes so as to emphasize structure on different size scales. X-ray images and radio overlays for each radio-galaxy environment are shown in Figs 1–6.

We carried out spectral analysis for several regions of each environment, as described in more detail in the following sections.

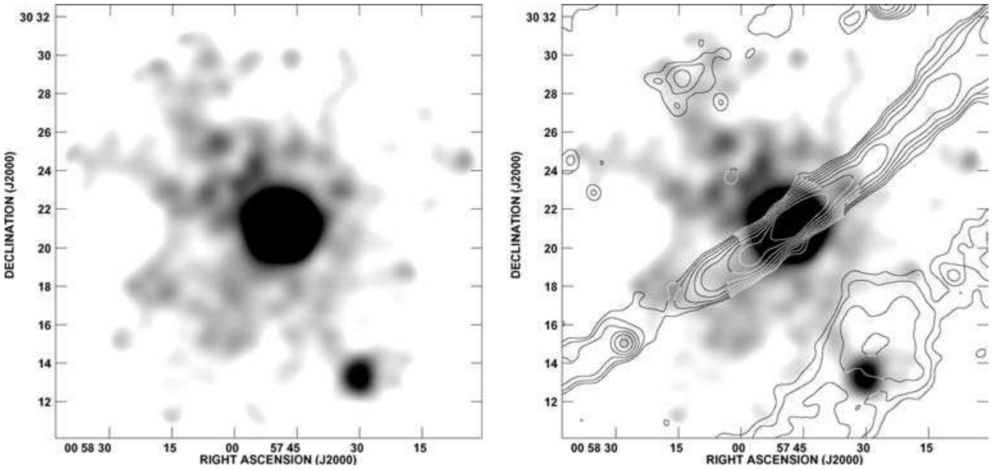

Figure 1. The X-ray environment of NGC 315. Images made from the combined MOS1, MOS2 and pn event lists in the 0.5–5.0 keV energy range, with exposure correction to correct for chip gaps but not vignetting, as described in the text. Left-hand panel: smoothed with a Gaussian of full width at half-maximum (FWHM) 33 arcsec to show the group-scale emission. Right-hand panel: with 1.4-GHz radio contours (Laing et al. 2006) overlaid.

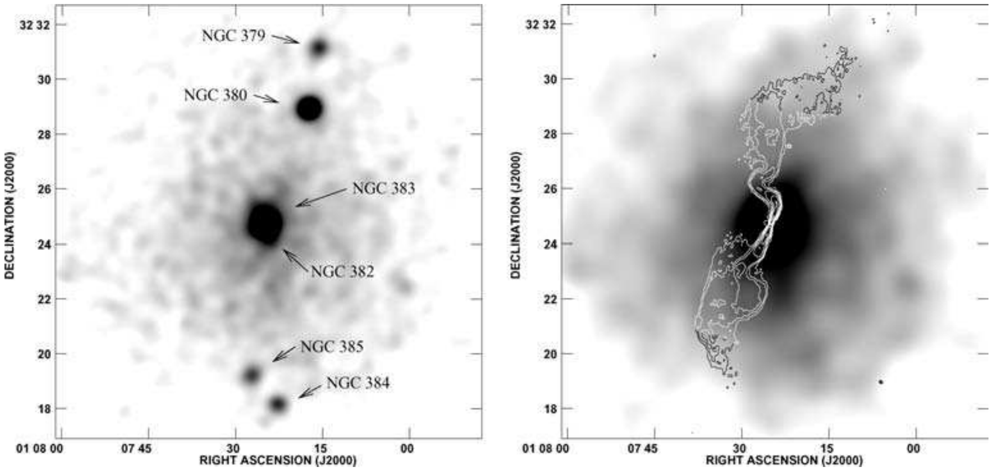

Figure 2. The X-ray environment of 3C 31. Images made from the combined MOS1, MOS2 and pn event lists in the 0.5–5.0 keV energy range, with exposure correction to correct for chip gaps but not vignetting, as described in the text. Left-hand panel: smoothed with a Gaussian of FWHM 13 arcsec to highlight the emission associated with several of the NGC 383 group galaxies. The central galaxy is NGC 383, with a slight elongation to the south-west due to emission from its companion galaxy NGC 382; right-hand panel: smoothed with a Gaussian of FWHM 26 arcsec to highlight the group-scale emission, and with galaxy emission removed, overlaid with 1.6-GHz radio contours (Laing et al. 2008).

Spectra were extracted using the SAS *evselect* task, with vignetting correction included by applying the event weights. We used a double-subtraction technique that makes use of filter-wheel closed observations, which provide high signal-to-noise ratio information about the particle and instrumental background as a function of spatial position.[1] To account for variations in the level of particle background between our observations and the filter-wheel closed data sets, the background events were scaled by the ratio of 10–12 keV (MOS) or 12–14 keV (pn) counts over the full field of view for the source and background data sets. Spectra were then extracted for source and local background extraction regions (typically a surrounding annulus) from both target and background events lists, with the background events scaled as explained above. The spectra extracted from the background events list were used as backgrounds for the corresponding target observation spectra. Appropriate response files were generated using *rmfgen* and *arfgen*. The target spectra for both the source and local background regions were grouped to a minimum of 20 counts per bin after background subtraction. The local background spectrum from the target observation was then used to determine the Galactic and cosmic X-ray background spectrum for our observation. By using the scaled filter-wheel closed spectrum for the same region as a background, the particle background is completely removed. We therefore fitted an X-ray background model to the local background spectrum consisting of two *mekal* models to account for emission from the Galactic bubble and a power-law model absorbed by the Galactic N_H in the direction of the target (see Table 6) to account for the cosmic X-ray background. The *mekal* temperatures were allowed to vary, but the power-law index was fixed at $\Gamma = 1.41$ (Lumb et al. 2002). The normalizations of all three components were allowed to vary. In all the cases, this model provided a good fit to the background spectrum of our target observations. For each source spectrum, we used the corresponding filter-

---

[1] See the *XMM–Newton* background analysis website at http://xmm.vilspa.esa.es/external/xmm_sw_cal/background/index.shtml.

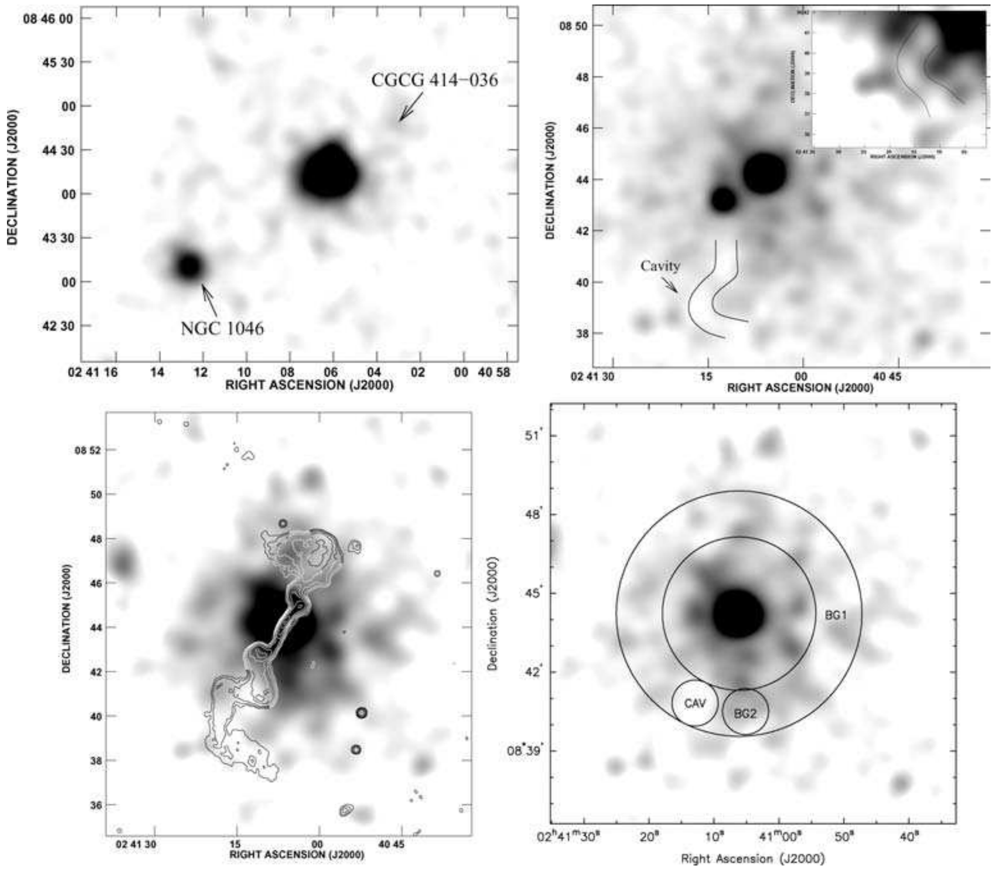

Figure 3. The X-ray environment of NGC 1044. Images made from the combined MOS1, MOS2 and pn event lists in the 0.5–5.0 keV energy range, with exposure correction to correct for chip gaps but not vignetting, as described in the text. Top left-hand panel: smoothed with a Gaussian of FWHM 13 arcsec to highlight the emission associated with several of the NGC 1044 group galaxies. Top right-hand panel: the same image smoothed with a Gaussian of FWHM 20 arcsec and with galaxy emission removed to show the group-scale emission and cavity to the S; an inset shows a close-up of the cavity region from an image smoothed with a Gaussian of FWHM 26 arcsec. Bottom left-hand panel: image smoothed with a Gaussian of FWHM 26 arcsec to highlight the group emission, with 1.4-GHz radio contours overlaid illustrating that the southern radio plume fills the cavity shown in the middle panel. Bottom right-hand panel: regions used to investigate significance of cavity detection.

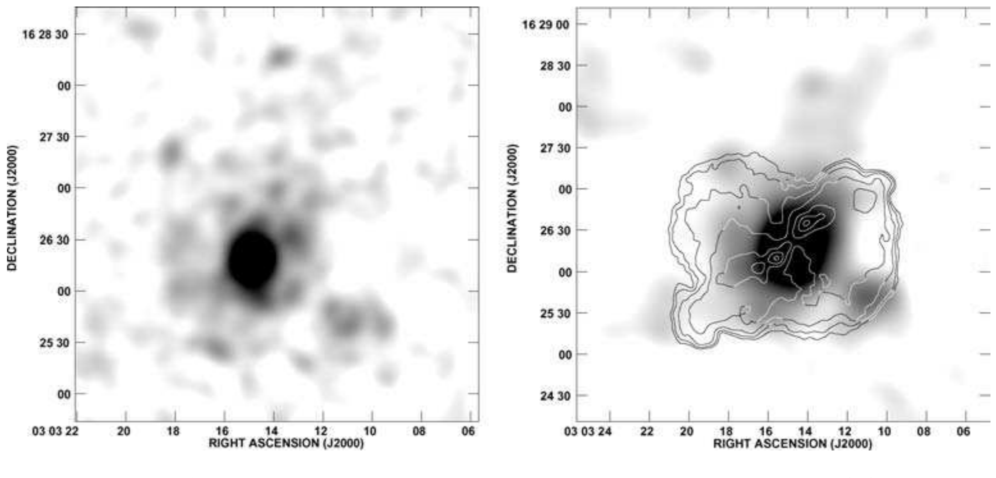

Figure 4. The X-ray environment of 3C 76.1. Images made from the combined MOS1, MOS2 and pn event lists in the 0.5–5.0 keV energy range, with exposure correction to correct for chip gaps but not vignetting, as described in the text. Left-hand panel: image smoothed with a Gaussian of FWHM 5.2 arcsec; right-hand panel: smoothed with a Gaussian of FWHM 10.4 arcsec and with 1.4-GHz radio contours overlaid.

wheel closed spectrum as a background spectrum, to account for particle background, and a fixed X-ray background model consisting of the best-fitting model for the particular observation, with the normalizations of each component fixed at the best-fitting values scaled to the appropriate area for the source extraction region. This method gave results consistent with other methods (double background subtraction using the background template files of Read & Ponman 2003 and local background subtraction), but in many cases the more accurate subtraction of both particle and X-ray background components afforded by this method enabled us to achieve

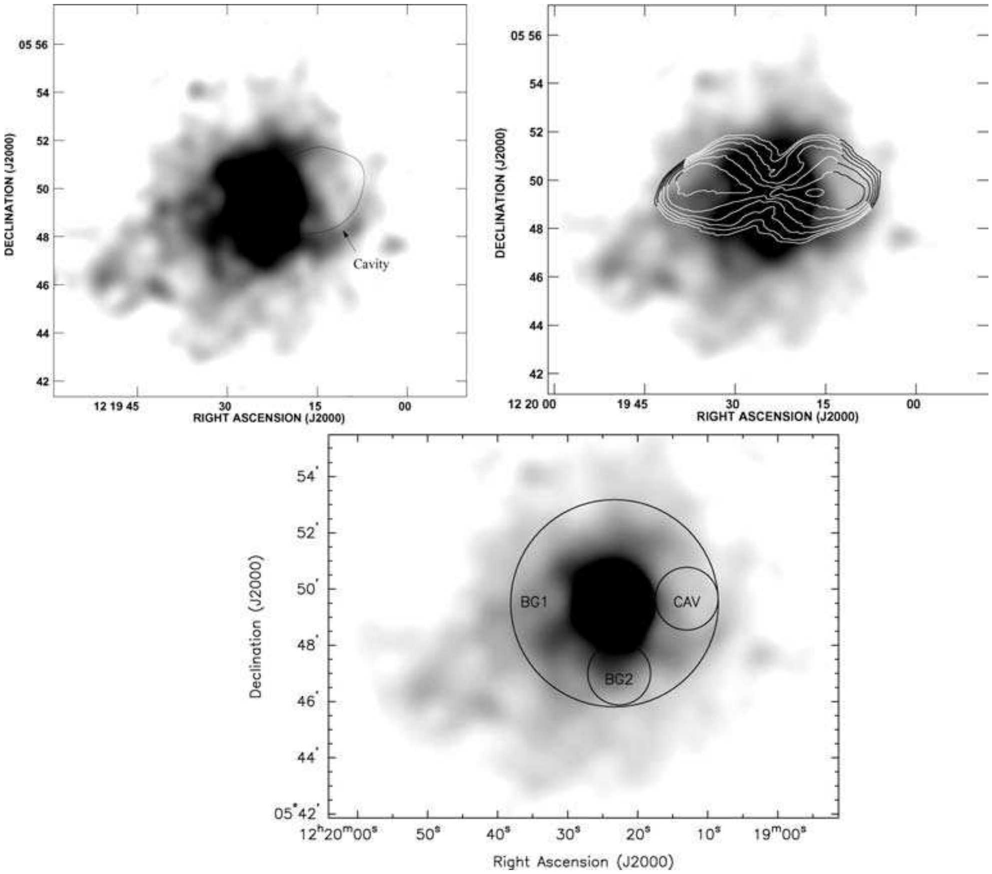

Figure 5. The X-ray environment of NGC 4261. Images made from the combined MOS1, MOS2 and pn event lists in the 0.5–5.0 keV energy range, with exposure correction to correct for chip gaps but not vignetting, as described in the text. Top left-hand panel: smoothed with a Gaussian of FWHM 26 arcsec and with galaxy emission removed to show the group-scale emission and cavity to the W; top right-hand panel: smoothed with a Gaussian of 33 arcsec and with 1.4-GHz radio contours overlaid illustrating that the W lobe coincides with the cavity in the group-scale gas; bottom panel: regions used to investigate significance of cavity detection.

significantly better constrained temperatures and abundances. Spectral fitting results are summarized in Table 3 and discussed in detail in Section 3.

2.3.2 *Spatial analysis*

Analysis of the gas distributions in each object was carried out using radial surface-brightness profiles, extracted in concentric annuli with point sources and chip gaps masked out. In all cases where resolved jets have been detected with *Chandra*, they are within the core radius of the point spread function (PSF) so that they can be considered to be part of the central point source, which is modelled as part of the surface-brightness profile analysis. Vignetting correction and double background subtraction using filter-wheel closed data sets were applied in the same manner as for the spectral analysis. The three surface-brightness profiles were fitted separately with models including point-source components, a single β model (e.g. Birkinshaw & Worrall 1993), and in some cases a model consisting of a line-of-sight projection of the sum of two β models in gas density, hereafter referred to as a *projb* model. The *projb* model is defined by

$$n(r) = n_0 \left[\left(1 + \frac{r^2}{r_{c,\mathrm{in}}^2}\right)^{-3\beta_{\mathrm{in}}/2} + N \left(1 + \frac{r^2}{r_c^2}\right)^{-3\beta/2} \right], \qquad (1)$$

where N is the relative normalization of the two β model components. The corresponding surface-brightness profile is determined via numerical integration of the following expression:

$$S_{\mathrm{X}}(R) \propto \int_{-\infty}^{\infty} n^2(l, R)\mathrm{d}l, \qquad (2)$$

where $r = (l^2 + R^2)^2$ is the radius, R is measured in the plane of the sky and l is along the line of sight. We explored the three- or six-dimensional parameter space for the β and *projb* models respectively, using a Markov-Chain Monte Carlo (MCMC) method.[2] We used the joint χ^2 value for the three profiles as the likelihood estimator and in the sections that follow we quote both the parameters of the best-fitting model and the Bayesian estimates for the value of each parameter. Plausible ranges for each parameter were estimated by carrying out extreme fits and these were used as priors for the MCMC method. The results of profile fits are given in Table 4 and the parameter ranges for each source are given in Table 5. Uncertainties (formally credible intervals: Gregory 2005) for each parameter are determined from the one-dimensional

---

[2] Our implementation of the MCMC method uses the Metropolis–Hastings algorithm in a manner very similar to the METRO code of Hobson & Baldwin (2004), but is implemented to run on a cluster of multiprocessor computers using the Message Passing Interface (MPI).

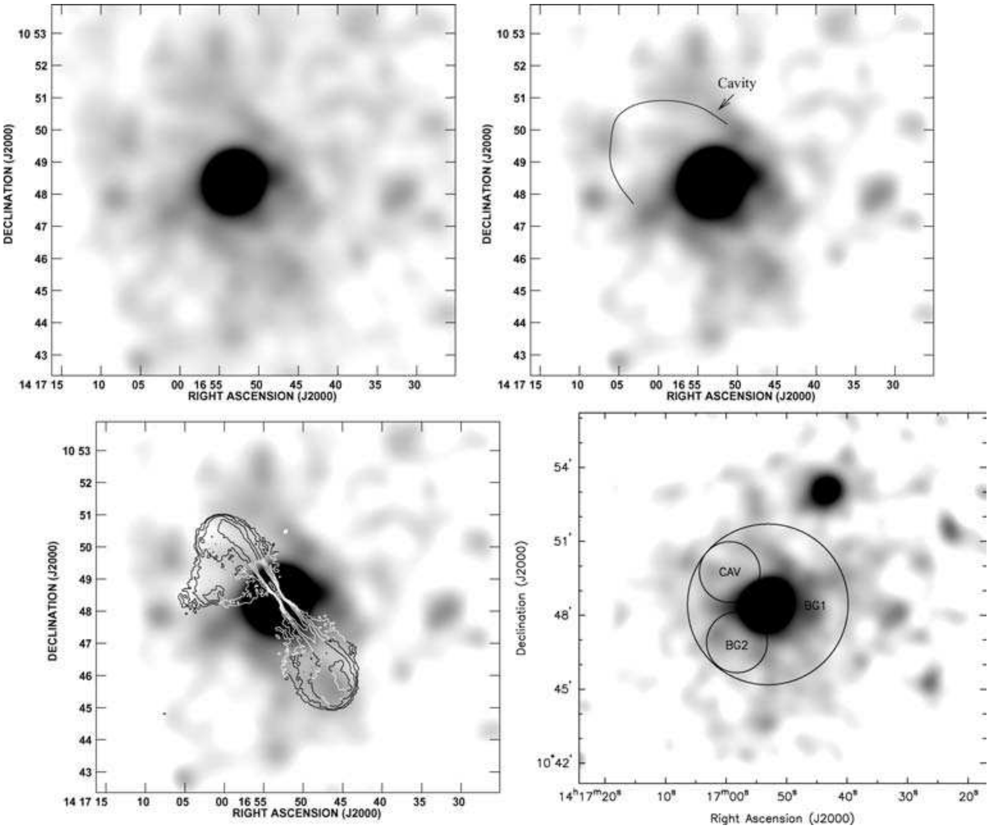

Figure 6. The X-ray environment of 3C 296. Images made from the combined MOS1, MOS2 and pn event lists in the 0.5–5.0 keV energy range, with exposure correction to correct for chip gaps but not vignetting, as described in the text. Images are smoothed with a Gaussian of FWHM 19 arcsec. Top left-hand panel: group emission; top right-hand panel: cavity to the NE highlighted; bottom left-hand panel: with 20-cm radio contours overlaid illustrating that the northern lobe fills the cavity seen in the top right-hand panel; bottom right-hand panel: regions used to investigate significance of cavity detection.

projection of the minimal n-dimensional volume that encloses 68 per cent of the posterior probability distribution as returned by the MCMC algorithm. The uncertainties determined in this way correspond to 1σ errors for two or five interesting parameters for the β and *projb* models, respectively. Quantities derived from the surface-brightness model fits, included X-ray luminosity and pressure at a given radius, are obtained by determining that quantity for each model fit and then obtaining the Bayesian estimate for the quantity in question. Uncertainties on the derived quantities come from the minimal one-dimensional interval that encloses 68 per cent of the posterior probability space for the given quantity, and so correspond to 1σ errors for a single parameter of interest in a traditional fitting procedure. As seen in Section 3, some of the parameters are strongly correlated, leading to large uncertainties on the individual model parameters; however, tight constraints can be obtained on derived quantities such as pressure and luminosity. Our method does not treat the model normalization as a free parameter, instead finding the best normalization for each model; however, the uncertainty in model normalization does not significantly affect the constraints on model parameters or derived quantities.

Before fitting, each model was convolved with the *XMM–Newton* PSF based on the on-axis parametrization described in the *XMM–Newton* CCF files XRT1_XPSF_0006.CCF, XRT2_XPSF_0007.CCF and XRT3_XPSF_0007.CCF. For three sources with *Chandra*-detected galaxy-scale environments with core radii too small to be resolved by *XMM–Newton* (NGC 315, 3C 296 and NGC 6251), we included previously published *Chandra* profiles in the combined fits so as to model the inner profiles as well as possible. Final pn surface-brightness profiles for each radio-galaxy environment with a model using the best-fitting model parameters, as discussed in the individual sections below, are shown in Fig. 7.

3 RESULTS

3.1 NGC 315

Images of the environment of NGC 315 are shown in Fig. 1. Emission is detected from NGC 315, the group galaxies NGC 311 and NGC 318, a candidate more distant cluster at $\alpha = 00^{\mathrm{h}}57^{\mathrm{m}}31^{\mathrm{s}}$, $\delta = +30^{\circ}13'$, which does not appear to have been identified previously, and the intragroup medium. The X-ray emission appears somewhat elongated to the north-east in a direction perpendicular to the radio jets . We measure a total of ~4000 0.3–7.0 keV pn counts from the galaxy and group environment. Although NGC 315 has previously been studied in detail with *ROSAT* and *Chandra*, this is the first detection of an environment on hundred-kpc scales. Unfortunately, this data set is also highly flare contaminated, with only 12–15 ks usable of a total observed 50 ks (see Table 6).

The results of surface-brightness profile fits for NGC 315 are given in Table 4. The inner environment of NGC 315 is well constrained from *Chandra* observations, and so in this case we

Table 3. Spectral fits to the large-scale group emission for each environment. Results are for joint fits to the three *XMM–Newton* cameras in the energy range 0.3–7.0 keV. Luminosities are the Bayesian estimates for the bolometric luminosities to a radius of r_{500} (see Table 6) with 1σ errors, as determined from our surface-brightness profile model fits.

Object	z	N_H (10^{20} cm^{-2})	kT (keV)	Z ($Z_\odot$)	χ^2 (d.o.f.)	log (L_X) (erg s^{-1})	Notes
NGC 315	0.016	5.88	$1.3^{+0.5}_{-0.3}$	0.3 (fixed)	117 (84)	41.89 ± 0.01	
3C 31	0.017	5.39	1.5 ± 0.1	0.35 (fixed)	25 (22)	43.10 ± 0.01	Results from OP04
3C 66B	0.0215	8.36	$1.73^{+0.03}_{-0.04}$	0.28 ± 0.03	819 (718)	$43.03^{+0.03}_{-0.11}$	See C03 for details
NGC 1044	0.021	8.76	$1.13^{+0.14}_{-0.06}$	$0.64^{+1.3}_{-0.22}$	375 (330)	42.13 ± 0.08	
3C 76.1	0.032	10.8	$0.91^{+0.25}_{-0.14}$	0.3 (fixed)	26.6 (25)	$41.39^{+0.02}_{-0.12}$	
NGC 4261	0.0073	1.55	$1.45^{+0.23}_{-0.01}$	$0.26^{+0.15}_{-0.04}$	1186 (819)	$42.07^{+0.21}_{-0.40}$	
3C 296	0.024	1.86	$0.90^{+0.10}_{-0.04}$	$0.14^{+0.06}_{-0.08}$	1071 (728)	$42.40^{+0.13}_{-0.29}$	
NGC 6251	0.0244	5.82	$1.6^{+0.5}_{-0.3}$	$0.4^{+0.7}_{-0.3}$	119 (109)	$41.93^{+0.02}_{-0.04}$	See E05 for details
3C 449	0.0171	11.8	0.98 ± 0.02	$0.13^{+0.01}_{-0.02}$	881 (441)	43.08 ± 0.04	See C03 for details

References: OP04 refers to Osmond & Ponman (2004); C03 refers to Croston et al. (2003) and E05 refers to Evans et al. (2005).

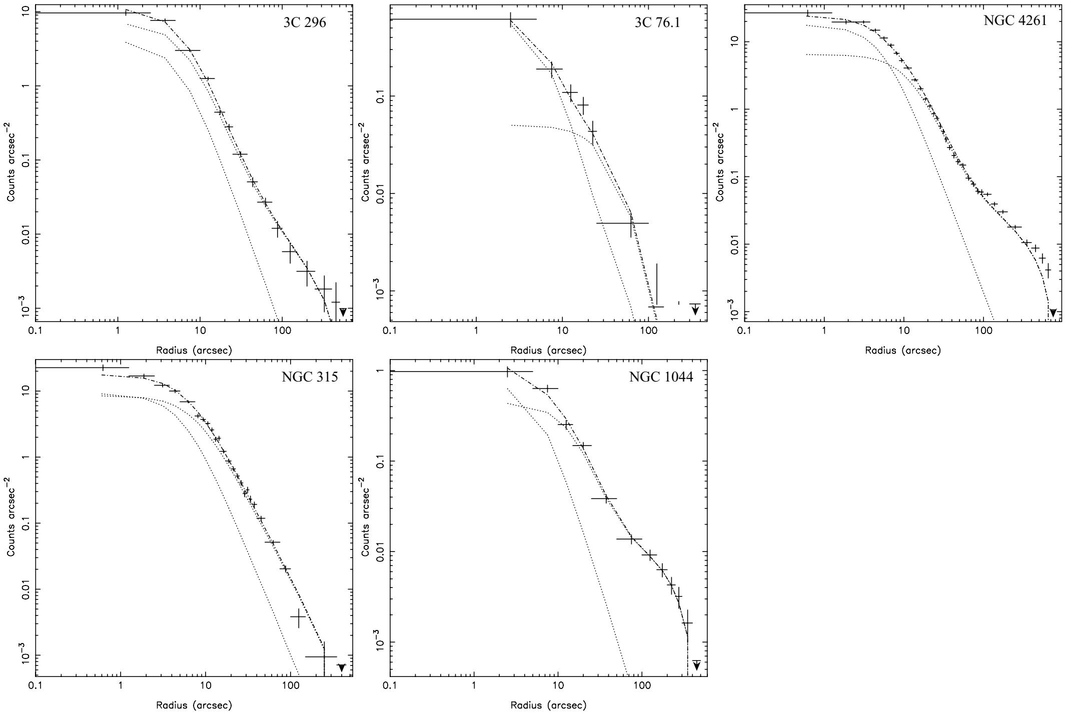

Figure 7. EPIC pn surface-brightness profile with best-fitting point source plus β model or *projb* model, as discussed in the text, for the newly observed galaxies. Top row (left- to right-hand side): the bridged sources 3C 296, 3C 76.1, NGC 4261; bottom row: the plumed sources NGC 315 and NGC 1044. (The somewhat poor fit in the outer regions for NGC 4261 is because the model is from the best joint fit, rather than the best fit to the pn profile alone).

carried out a joint fit to four profiles: one for each *XMM–Newton* camera, plus the *Chandra* profile of Worrall et al. (2007). As shown in Fig. 7, the profile of NGC 315 does not appear to flatten into a group-scale component on hundred kpc scales, unlike the majority of other FR I environments known to date, and so the *projb* model was not required to fit its surface-brightness profile. As shown in Table 4, the preferred β model parameters are in agreement at the joint 1σ level with the parameter values measured from the *Chandra* data alone by Worrall et al. (2007) ($\beta = 0.52 \pm 0.01$ and $r_c = 1.7 \pm 0.2$ arcsec).

We extracted a spectrum in the inner 60 arcsec to study the core emission from NGC 315 and found that the *Chandra* best-fitting model consisting of an absorbed power law with $N_H = 7.6 \times ^{10^{21}\,\mathrm{cm}^{-2}}$ and $\Gamma = 1.57$ plus a *mekal* model with $kT = 0.62 \pm 0.02$ keV and abundance fixed at 0.3 solar was a good fit [$\chi^2 = 155$ for 125 degrees of freedom (d.o.f.)]. The results of fitting to the group emission in a region between 120 and 300 arcsec are given in Table 3.

In order to obtain profiles of gas density and pressure, we assumed a linear ramp in gas temperature obtained by fitting a straight line to the *Chandra* temperature profile of Worrall et al. (2007) and the *XMM–Newton* temperature data point. The temperature was held constant at the *XMM–Newton*-measured value beyond 217 arcsec. Errors on profiles take into account both the uncertainty in model parameters and the uncertainty in temperature.

We were also able to extract spectra for the group member galaxy NGC 311. The spectra were well fitted by a *mekal* model with

Table 4. Results of surface-brightness profile fits. For each parameter, we list the parameter value from the fit with the minimum χ^2 and the Bayesian parameter estimate together with credible intervals taking into account all fit parameters. Column 2 gives the model normalizations in electron density for the best fit in units of 10^3 m^{-3} – note that for the *projb* model this does not correspond exactly to the density at zero radius. Radii are given in units of arcsec.

Object	Best fit							Bayesian estimate				
	$n_{e,0}$	β	r_c	$\beta_{\rm in}$	$r_{\rm c,in}$	N	χ^2 (d.o.f.)	β	r_c	$\beta_{\rm in}$	$r_{\rm c,in}$	N
NGC 315	400	0.54	2.12	–	–	–	186 (126)	$0.54^{+0.02}_{-0.01}$	$2.13^{+0.45}_{-0.39}$	–	–	–
3C 66B	12	1.2	428.2	1.2	17.6	0.083	470 (230)	$0.91^{+0.29}_{-0.47}$	367^{+103}_{-155}	$1.1^{+0.1}_{-0.4}$	$16.4^{+3.6}_{-10.1}$	$0.094^{+0.3}_{-0.07}$
NGC 1044	14	1.2	416	0.84	13.3	0.0225	38.2 (28)	$0.81^{+0.39}_{-0.51}$	356^{+640}_{-255}	$0.88^{+0.32}_{-0.35}$	$14.2^{+5.8}_{-9.3}$	$0.0243^{+0.0254}_{-0.0185}$
3C 76.1	2.6	0.94	42.1	–	–	–	11.3 (16)	0.9*	43*	–	–	–
NGC 4261	77	0.30	243.6	0.64	7.0	0.004 43	156 (100)	0.62*	482*	$0.64^{+0.35}_{-0.14}$	$7.0^{+3.0}_{-4.3}$	0.0046*
3C 296	720	0.31	77.5	0.60	0.95	0.000 0446	80.5 (92)	0.67*	545*	$0.58^{+0.07}_{-0.03}$	$0.86^{+0.44}_{-0.31}$	$0.000\,21^{+0.0008}_{-0.0001}$
NGC 6251	38	1.1	150	1.2	9.9	0.044	160 (139)	$1.0^{+0.2}_{-0.5}$	138^{+76}_{-82}	0.96*	8.1*	0.053 ± 0.050
3C 449	3.7	0.42	57.1	–	–	–	457 (273)	$0.42^{+0.06}_{-0.05}$	58^{+19}_{-16}	–	–	–

*Unconstrained within the parameter range explored. See Table 5.

$kT = 1.4^{+0.6}_{-0.3}$ keV with abundance fixed at 0.3 times solar ($\chi^2 = 1.2$ for 3 d.o.f.) or by a power law with $\Gamma = 2.6 \pm 0.5$ ($\chi^2 = 1.6$ for 3 d.o.f.). The data are insufficient for distinguishing between the two models; however, the temperature of the thermal fit is higher than would be expected for a galaxy atmosphere, and so it is likely that some of the emission is associated with nuclear activity or X-ray binaries.

3.2 3C 31

Fig. 2 shows images of the environment of 3C 31 from our new *XMM–Newton* observation. Emission is detected from several group galaxies as well as from the intragroup medium. Unfortunately, the observations of 3C 31 were severely flare contaminated making quantitative analysis extremely difficult. After preliminary analysis we concluded that it was not possible to estimate reliably the level of background for this observation and so we did not carry out either spectral or spatial analysis. 3C 31 has been studied in detail with *ROSAT* (Komossa & Böhringer 1999) and *Chandra* (Hardcastle et al. 2002). For comparisons with the other radio galaxies in this sample, we therefore made use of the results of those two studies. A forthcoming re-observation with *XMM–Newton* will allow a much more detailed study of 3C 31's environment and environmental interactions.

3.3 NGC 1044

The environment of NGC 1044 is shown in Fig. 3. This data set was relatively free of flare contamination, and a total of ~7840 0.3–7.0 keV pn counts are detected from the environment. Fig. 3 reveals a cavity at the position of the south-east (SE) lobe. We tested the statistical significance of the surface-brightness deficit by comparing the total (MOS1 + MOS2 + pn) surface brightness in a circle of radius 53 arcsec defined using the radio map, an annular background centred on the nucleus of NGC 1044 extending from the inner to the outer edge of the cavity region, but excluding the SE quadrant, and a background of the same size rotated about the centre of the environment. The cavity has a surface brightness of 0.0247 ± 0.0017 counts arcsec^{-2}, compared to a surface brightness of 0.0315 ± 0.0005 counts arcsec^{-2} in the annular background region and a surface brightness of 0.0398 ± 0.0022 counts arcsec^{-2} in the same-sized background region. The errors on surface-brightness measurements were obtained by combining in quadrature source and background errors determined from the Poissonian errors on the counts in each region. The deficit is significant at a level $>3\sigma$.

NGC 1044 has not previously been observed in the X-ray, and so its inner (galaxy scale) environment is not well constrained. Our new observations provide the first detection of an X-ray environment for this radio galaxy. The surface-brightness profile for NGC 1044 (Fig. 7) shows a characteristic two-component shape indicating the presence of a central AGN or galaxy-scale component as well as a large-scale group gas component. A point source plus single β model is a poor fit to the profiles, and so we used a point source plus *projb* model, with model fitting results given in Table 4. Results of a spectral fit to the group-scale emission in an annulus between 100 and 400 arcsec are given in Table 3.

Although the surface-brightness profile does not show evidence for a dominant AGN component, we extracted spectra from a source-centred circle of 1 arcmin radius to investigate the contributions of AGN and galaxy-scale gas-related emission. Consistent with the surface-brightness profile results, we found that a single power-law model did not provide an acceptable fit to the data. We obtained a good fit ($\chi^2 = 40$ for 37 d.o.f.) for a single *mekal* model with $kT = 0.82 \pm 0.05$ keV and $Z = 0.15^{+0.6}_{-0.05}\ Z_{\odot}$. A somewhat better fit was obtained for a two-component *mekal* plus power-law model ($\chi^2 = 32.3$ for 36 d.o.f.) with $kT = 0.77^{+0.05}_{-0.04}$ keV, abundance fixed at 0.5 times solar and $\Gamma = 1.91^{+0.34}_{-0.42}$. The single *mekal* model gives an unabsorbed 0.1–10 keV luminosity of $(1.3 \pm 0.2) \times 10^{41}$ erg s^{-1}, which is high for a galaxy atmosphere, whereas we obtain a more reasonable luminosity of 7.5×10^{40} erg s^{-1} for the combined fit. The combined fits give a 1-keV flux density of 6 ± 1 nJy for the power-law component, which is consistent with the nuclear X-ray emission predicted by the relation of Evans et al. (2006) for a source of NGC 1044's core radio flux density (<0.08 Jy at 1.5 GHz).

We used the surface-brightness profile models and the measured temperature to determine profiles of gas density and pressure by using the best-fitting *projb* model parameters to obtain an emission measure profile. As we were unable to obtain a temperature profile for this group, we assumed the gas is isothermal with the spectral parameters of the best fit to the group spectrum ($kT = 1.3$ keV and $Z = 0.12$ solar) in order to obtain gas density and pressure profiles. Errors on the density and pressure profiles were determined by combining in quadrature the 1σ confidence range from the dispersion in profile fits with the uncertainty in temperature as for the other sources.

Of the NGC 1044 group galaxies, X-ray emission is clearly detected from NGC 1046 ($z = 0.0199$) and CGCG414–036 ($z = 0.0206$) as shown in Fig. 3. We were able to extract spectra for NGC 1046, and fitted *mekal*, single power-law and *mekal* plus power-law models. All three models gave good fits to the spectra; however, the best-fitting single *mekal* model ($\chi^2 = 4.2$ for 6 d.o.f.) required low abundance ($Z < 0.04\ Z_{\odot}$) and the best-fitting power-law model ($\chi^2 = 1.8$ for 7 d.o.f.) required a steep photon index ($\Gamma = 3.2^{+0.4}_{-0.5}$). We obtained the lowest reduced χ^2 and most physically plausible parameters for the two-component fit ($\chi^2 = 0.8$ for 5 d.o.f.) with $kT = 0.2^{+0.3}_{-0.1}$ keV and $\Gamma = 2.3^{+1.3}_{-0.7}$ and abundance fixed at 0.5 times solar. We conclude that there is likely to be some non-thermal emission associated with this galaxy, either associated with X-ray binaries or nuclear activity, in addition to thermal emission from a galaxy atmosphere. There were insufficient counts associated with CGCG414–036 to extract a useful spectrum.

3.4 3C 76.1

This observation is the first pointed X-ray observation of 3C 76.1. As shown in Fig. 4, the environment of 3C 76.1 is considerably poorer than those of the other radio galaxies in this sample. The X-ray emission appears elongated in the north-south (NS) direction, perpendicular to the radio lobes. We detect a total of ~385 0.3–7.0 keV pn counts from the group environment.

To confirm the presence of extended emission, we fitted a point source-only model to this surface-brightness profile (which is shown in Fig. 7). This did not give an acceptable χ^2, whereas we were able to obtain good fits with a point source plus β model, as listed in Table 4. As the profiles are inconsistent with a point source only model, and the β-model fit is good, we conclude that 3C 76.1's environment has been firmly detected for the first time. As discussed below, the point-source component appears to originate partly from a central AGN and partly from an unresolved galaxy-scale atmosphere.

We list the results of a spectral fit to the group emission in the region between 30 and 200 arcsec in Table 3. We used a fixed abundance as the abundance value tended to unrealistically high values if left free. We used the fitted surface-brightness profile model and the measured temperature to determine profiles of gas density and pressure. As for NGC 1044, we assumed the gas to be isothermal with the spectral parameters of the best fit to the group spectrum ($kT = 0.91$ keV and $Z = 0.3$ solar) in order to obtain gas density and pressure profiles. Errors on the profiles were determined as for the other sources described above.

To constrain the origin of the unresolved central emission, we extracted a spectrum in the central 30 arcsec using local background to subtract off the contribution from the group-scale emission. We found that neither a power law nor a *mekal* model on their own gave an acceptable fit, and so we fitted a power-law plus *mekal* model, which gave a χ^2 value of 15.5 for 12 d.o.f. with $kT = 0.43^{+0.16}_{-0.11}$ keV (for abundance fixed at 0.3 times solar) and $\Gamma = 0.9^{+0.2}_{-0.3}$. Such a flat power-law index suggests that an absorbed power-law component, as commonly seen in narrow-line radio galaxies (Hardcastle, Evans & Croston 2006) and in some low-power sources such as NGC 3801 (Croston et al. 2007), may be present.

3.5 NGC 4261

The environment of NGC 4261 is shown in Fig. 5. The inner environment of this radio galaxy as observed by *Chandra* was discussed by Zezas et al. (2005), Croston et al. (2005a), where we also presented an image of the *XMM–Newton* data but not a detailed analysis, and Jetha et al. (2007). We detect a total of ~33 000 0.3–7.0 keV pn counts from the source, including a contribution from the central AGN. The data set is not significantly contaminated by flares.

Fig. 5 reveals a cavity at the position of the W lobe. We tested the statistical significance of the surface brightness deficit by comparing the total (MOS1 + MOS2 + pn) surface brightness in a circle of radius 67 arcsec defined using the radio map with an annular background region centred on the nucleus of NGC 4261 extending from the inner to the outer edge of the cavity region, but excluding the SE quadrant, and with a background of the same size as the cavity region but rotated about the centre of the group to the S. The cavity has a surface brightness of 0.0942 ± 0.0027 counts arcsec^{-2}, compared to a surface brightness of 0.1081 ± 0.0011 counts arcsec^{-2} in the annular background region and a surface brightness of 0.1434 ± 0.003 counts arcsec^{-2} in the same-sized background. Hence, the deficit is significant at a level between 3 and 8σ. The errors on the surface-brightness measurements were obtained as for NGC 1044. There is no statistically significant large-scale cavity on the eastern side of the source; however, there is evidence for a smaller region of lower surface-brightness deficit close to the nucleus and coincident with the inner parts of the eastern radio lobe.

As shown in Fig. 7, the surface-brightness profile shows a two-component form with a large-scale component in addition to a galaxy-scale inner environment (e.g. Zezas et al. 2005). We therefore fitted the point source plus *projb* model as for NGC 1044. The results are listed in Table 4. Table 3 gives the results of spectral fitting to the group-scale emission between 60 and 600 arcsec. We were concerned that because the physical scales we are sampling in NGC 4261 are considerably smaller than in the other sources in our sample (due to its lower redshift) contamination from X-ray binaries in the galaxy could be a problem ($D_{25} = 4.1$ arcmin for NGC 4261, whereas it is <2 arcmin for most of the other galaxies – here, D_{25} is the optical radius of the galaxy at a B-band surface brightness of 25 mag arcsec^2), and so we included a thermal bremsstrahlung component with $kT = 5.0$ keV to account for an X-ray binary population; however, for the global spectrum this component was not significant. We investigated whether a temperature gradient is present by extracting spectra in several annuli. For the outer two bins, the normalization of the included thermal bremsstrahlung component was negligible, consistent with the expectation of no contribution from binaries on those scales. In the inner two regions (which are both within the D_{25} radius of the galaxy), the bremsstrahlung component contained a significant fraction of the total flux, corresponding to a total X-ray binary 0.3–8 keV luminosity of $\sim 3 \times 10^{40}$ erg s^{-1}. This is consistent with the expectation for NGC 4261 based on the mean $L_{\rm X}$–$L_{\rm B}$ relation of Kim & Fabbiano (1994). We found no evidence of a significant temperature gradient when the X-ray binary contribution is accounted for.

We also extracted spectra from a source-centred circle of 1 arcmin radius in order to investigate the AGN and galaxy-scale X-ray emission. We found that neither a single *mekal* nor a single power-law model provided an acceptable fit. We then fitted a *mekal* plus power-law model, which gave a reasonable fit statistic ($\chi^2 = 503$ for 408 d.o.f.) for $kT = 0.65^{+0.01}_{-0.02}$ keV and abundance fixed at 0.5 times solar; however, the best-fitting power-law index is very flat: $\Gamma = 0.57 \pm 0.11$. We therefore tried fitting the best-fitting model of Zezas et al. (2005) (their Model 5). If we fix the column densities, power-law indices and Raymond–Smith temperature to their best-fitting values, we cannot obtain an acceptable fit; however, allowing the temperature to vary gives a good fit with $\chi^2 = 585$ for 406 d.o.f. for a temperature of $kT = 0.69 \pm 0.01$ keV. The higher temperature is likely to be due to the larger extraction region used here, which is likely to include hotter gas from outer regions of the galaxy atmosphere and/or a contribution from X-ray binaries.

Two other galaxies in the NGC 4261 group were detected with sufficient counts to carry out spectral fitting, NGC 4254 ($z = 0.016$) and PCG 039660 ($z = 0.017$). We fitted single *mekal* and power-law fits to each galaxy (the statistics were too poor to allow fitting of more complex models). For NGC 4254, we found good fits with both models, with a slightly better fit statistic ($\chi^2 = 5.9$ for 4 d.o.f.) for the *mekal* model, but a temperature of > 1.3 keV, which is high for a galaxy atmosphere. The best-fitting power-law model ($\chi^2 = 6.6$ for 4 d.o.f.) had $\Gamma = 1.4^{+0.6}_{-0.5}$. It seems likely that the emission from this galaxy is at least partly non-thermal in origin. For PCG 039660, the *mekal* model was unacceptable, whereas the power-law model was a good fit ($\chi^2 = 2.0$ for 2 d.o.f.) with $\Gamma = 1.6^{+0.5}_{-0.6}$, and so we conclude that its emission is predominantly non-thermal.

3.6 3C 296

As shown in the left-hand panel of Fig. 6, 3C 296 possesses a group environment of moderate X-ray surface brightness. This is the first detection of a group-scale environment for this radio galaxy. We measure a total of ∼6800 0.3–7.0 keV pn counts from the group environment.

Fig. 6 reveals a cavity at the position of the NE lobe. We tested the statistical significance of the surface-brightness deficit by comparing the total (MOS1 + MOS2 + pn) surface brightness in a circle of radius 74 arcsec defined using the radio map, in an annular background region centred on the nucleus of 3C 296 extending from the inner to the outer edge of the cavity region, but excluding the NE quadrant, and in a same-sized circular region rotated about the centre of the group to the S. The cavity has a surface brightness of 0.0736 ± 0.002 counts arcsec^{-2}, compared to a surface brightness of 0.0870 ± 0.001 counts arcsec^{-2} in the annular background region and a surface brightness of 0.0927 ± 0.002 counts arcsec^{-2} in the same-sized region. The errors on the surface-brightness measurements were obtained as for NGC 1044. Hence, the deficit is significant at a level of $\sim 4.5\sigma$.

3C 296 has previously been observed with *Chandra* (Hardcastle et al. 2005). These observations revealed the presence of a galaxy-scale hot-gas component with $kT = 0.7$ keV extending to distances of ∼1 arcmin. This component dominated over the compact emission associated with the AGN beyond ∼1 arcsec. Our *XMM–Newton* surface-brightness profile for 3C 296 (top left-hand panel of Fig. 7) is dominated by the galaxy-scale component to a distance of ∼60 arcsec, beyond which the profile flattens slightly.

As for NGC 315, we carried out a joint fit to the *Chandra* and *XMM–Newton* profiles for 3C 296, so as to provide the best possible constraints on both the inner and the outer gas properties. A single β model is an unacceptable fit to the profiles, due to the excess of emission at large radii. We therefore used the point-source plus *projb* model to model both the inner and the outer components, finding good fits, as listed in Table 4. The inner parameters we measure are in good agreement with the best-fitting parameters of a single β model fitted to the *Chandra* profile alone, $\beta = 0.56 \pm 0.01$ and $r_c = 0.7^{+0.14}_{-0.10}$ arcsec (Hardcastle et al. 2005). Table 3 lists the results of a spectral fit to the group emission in the region between 50 and 400 arcsec. As the fit is comparatively poor, we extracted spectra in concentric annuli to investigate whether a temperature gradient is present. The temperature was found to decrease from ∼1.4 keV towards the centre to ∼0.9 keV in the outer regions; however, the temperatures are consistent within the errors, so that no significant gradient can be claimed. We used the fitted surface-brightness profile model to determine profiles of gas density and pressure, assuming an isothermal atmosphere. Density and pressure profiles, and their uncertainties were determined as for the other sources. While the *Chandra* observation of 3C 296 showed a significant temperature gradient in the inner regions of the galaxy-scale emission, the inner temperature beyond 4 arcsec differs by at most 10 per cent from the *XMM–Newton* global temperature, and so this difference is accounted for by the comparatively large uncertainty of the *XMM–Newton* global temperature, which we include in the pressure profile uncertainties.

We also extracted a spectrum for the core region and for the nearby group galaxy NGC 5531 ($z = 0.026$), shown to the NE in Fig. 6. As found by Hardcastle et al. (2005), a power law with only Galactic absorption was not a good fit to the core spectra. In good agreement with the *Chandra* results, we found a good fit to an absorbed power-law plus *mekal* model, with $kT = 0.74^{+0.3}_{-0.5}$ keV, $N_H = (2 \pm 1) \times 10^{21}$ cm^{-2} and $\Gamma = 1.6 \pm 0.4$. The gas temperature is somewhat higher than that measured by *Chandra*, which is not surprising as our region encompasses more of the galaxy atmosphere, which is hotter on scales of tens of kpc. For NGC 5531, we found a good fit to a thermal model, with $kT = 0.60^{+0.12}_{-0.14}$ keV and $Z = 0.2^{+0.7}_{-0.1} Z_{\odot}$ ($\chi^2 = 17.2$ for 14 d.o.f.), in contrast to the results with *Chandra*, which required the inclusion of the power-law component. When a power-law component was included, its normalization tended to negligible values, and the fit was not improved. We measure an unabsorbed 2–10 keV flux density of factor of ∼17 lower than that reported by Hardcastle et al. (2005), and so variability of an AGN component may be the explanation for the differing spectral results.

We can use the observed cavity associated with the eastern lobe to obtain an estimate for the jet power for 3C 296. If we use the sound crossing time to the edge of the lobe (2×10^8 yr) as an upper limit on the source age, and calculate the energy required to inflate the lobe as $4P_{\rm mid}\,V$, where $P_{\rm mid}$ is the external pressure at the mid-point of the lobe (see Table 6), and V is the volume estimated from the extent of radio-lobe emission (this is preferable to estimating the cavity size directly from the X-ray data, due to *XMM–Newton*'s spatial resolution and the need for smoothing of the X-ray data to reveal the cavity structure), we find that the energy required to inflate the lobe is $\sim 3.9 \times 10^{51}$ J (3.9×10^{58} erg), corresponding to a jet power of 1.2×10^{36} W (1.2×10^{43} erg s^{-1}) for the two jets, assuming the western jet has the same power. This inferred jet power is roughly an order of magnitude higher than the X-ray luminosity of the 3C 296 group, so that significant heating is occurring in addition to the energy input required to balance radiative losses. The cavity properties are within the range shown in fig. 8 of McNamara & Nulsen (2007), but lie to the high cavity power side of the cavity power/X-ray luminosity distribution. This jet power estimate is an order of magnitude lower than the estimate for 3C 31 from the kinematic model of Laing & Bridle (2002a), which is somewhat surprising given that 3C 296 has a higher luminosity at 178 MHz (see Table 6). The sound crossing time is likely to be an overestimate of the lobe expansion time, as the lobes appear to be slightly supersonic in their outer regions at the present time, and were probably more highly overpressured at earlier times. Hence, our calculation of the

Table 5. Bayesian priors for the surface-brightness profile fits. Priors in core radius (arcsec) and relative normalization were determined individually for each source by finding extreme fits that gave poor χ^2 values.

Object	$\beta_{\rm min}$	$\beta_{\rm max}$	$r_{\rm c,min}$	$r_{\rm c,max}$	$\beta_{\rm in,min}$	$\beta_{\rm in,max}$	$r_{\rm cin,min}$	$r_{\rm cin,max}$	$N_{\rm min}$	$N_{\rm max}$
NGC 315	0.3	1.2	1	20	–	–	–	–	–	–
3C 66B	0.3	1.2	75	1000	0.3	1.2	1	30	0.001	0.5
NGC 1044	0.3	1.2	50	1000	0.3	1.2	0.5	20.0	0.0005	0.02
3C 76.1	0.3	1.2	2	100	–	–	–	–	–	–
NGC 4261	0.3	1.2	50.0	2000	0.3	1.2	0.1	10.0	0.000 01	0.001
3C 296	0.3	1.2	50	1000	0.3	1.2	0.1	10.0	0.000 01	0.001
NGC 6251	0.3	1.2	15	500	0.3	1.2	15	500	0.0001	0.1
3C 449	0.3	1.2	10	200	–	–	–	–	–	–

Table 6. Properties of the radio galaxies and their group environments.

Object	L_{178}	D	$r_{\rm ax}$	V	r_{500}	P_E	P_M	$P_{\rm int}$	R_E	R_M	$E_{\rm req}$	$E_{\rm rg}$
NGC 315	23.38	1000	0.14	65.35	512	−14.13	−13.64	−14.70	3.7	11.4	$52.86^{+0.22}_{-0.51}$	52.31
3C 31	23.96	307	0.16	63.85	558	−13.16	−12.60	−13.53	2.3	8.5	$52.99^{+0.2}_{-0.5}$	51.85
3C 66B	24.34	296	0.35	64.27	603	−12.46	−12.22	−13.33	7.4	12.9	$52.83^{+0.15}_{-0.23}$	52.65
NGC 1044	23.26	306	0.30	63.82	473	−13.25	−12.98	−13.82	3.7	6.9	$52.11^{+0.11}_{-0.16}$	51.44
3C 76.1	24.40	126	0.71	63.98	418	−13.12	−12.58	−13.21	1.2	4.3	$51.99^{+0.14}_{-0.21}$	52.00
NGC 4261	23.67	81	0.50	63.00	545	−12.51	−12.24	−13.04	3.4	6.3	$51.92^{+0.08}_{-0.09}$	51.36
3C 296	24.16	212	0.46	64.25	415	−13.25	−12.98	−13.28	1.1	2.0	<52.11	51.87
NGC 6251	24.08	1900	0.24	66.08	577	−14.63	−13.83	−15.70	12.0	74	$52.80^{+0.15}_{-0.22}$	52.85
3C 449	23.81	533	0.26	64.19	436	−13.17	−12.80	−13.81	4.4	10.2	–	51.99

Columns: 1. Radio-source or galaxy name; 2. Logarithm of the 178-MHz radio luminosity (W Hz^{-1} sr^{-1}); 3. Radio source projected physical size (kpc); 4. Axial ratio at widest part of radio source; 5. Logarithm of the sum of the volumes of the two lobes (m^3), determined by assuming a spherical or cylindrical volume based on the extent of the radio emission; 6. r_{500}, the radius enclosing a mean density of 500 times $\rho_{\rm crit}$, determined using the relation of Arnaud, Pointecouteau & Pratt (2005) (kpc); 7. Logarithm of the thermal gas pressure at the outer edge of the radio lobes , averaged for the two lobes except in the cases of NGC 315 and NGC 6251 (Pa); 8. Logarithm of the thermal gas pressure at the midpoint of the radio lobes, averaged for the two lobes except in the cases of NGC 315 and NGC 6251 (Pa); 9. Logarithm of the internal equipartition pressure, averaged for the two lobes except in the cases of NGC 315 and NGC 6251 (Pa); 10. Average pressure ratio at the lobe endpoints; 11. Average pressure ratio at the lobe midpoint; 12. Logarithm of the energy required to produce the observed temperature offset from the RQ $L_{\rm X}$–$T_{\rm X}$ relation (J) (errors take into account uncertainties in the observed and predicted temperatures); 13. Logarithm of the energy available from the current episode of radio-galaxy activity ($4P_M V$, J).

energy input from 3C 296 discussed above may be an underestimate of the true value.

4 RESULTS FOR 3C 66B, 3C 449 AND NGC 6251

For the three radio galaxies where we have previously published detailed analyses of the environmental properties as probed by *XMM–Newton*, we chose to make use of the results published in Croston et al. (2003) and Evans et al. (2005), where very similar analysis procedures were used. In Table 3, we list the global gas properties obtained from single thermal model fits to the group gas as reported in these references. To enable a fair comparison with the pressure profiles for the newly observed objects, we refitted the surface-brightness profiles for the three previously observed sources with the point-source plus *projb* model where an inner component is detected (3C 66B and NGC 6251) or a point-source plus β model (3C 449) and used the MCMC method, which improves the sampling of parameter space. For NGC 6251, we included the *Chandra* profile of Evans et al. (2005) to constrain the small core-radius inner component. The results of these fits are listed in Table 4. We note that the quality of the fits for 3C 66B and 3C 449 is poor, as was the case for the single β model fits to the outer regions reported in Croston et al. (2003). We attribute this to the very high signal-to-noise ratio data for these two sources, for which real small-scale deviations in the gas distributions may be affecting the quality of the fit.

5 DISCUSSION

Table 6 summarizes the group properties as measured from the *XMM–Newton* data. The three previously studied radio-galaxy environments are included, with properties taken from Croston et al. (2003) and Evans et al. (2005). Properties of the radio galaxies obtained from the radio maps and from the literature are also included for comparison. It is clear from these results and from Table 3 (and can also be seen from the X-ray images) that the low-power radio galaxies in this ‘representative’ sample inhabit a wide range of environments, with bolometric X-ray luminosities spanning nearly two orders of magnitude from ∼10^{41} to 10^{43} erg s^{-1}, consistent with earlier results (Worrall & Birkinshaw 2000). The result is important for theoretical models of radio-galaxy evolution and environmental impact, as it has sometimes been assumed by modellers that environmental properties do not vary significantly.

In the following sections, we discuss the relationship between environmental properties and radio structure, source dynamics and particle content.

5.1 Relationship between properties of the radio galaxy and the environment

The importance of jet/environment interactions for group and cluster gas has been highlighted by the large number of X-ray cavity systems now known, ranging from elliptical galaxies to the richest clusters (e.g. Böhringer et al. 1993; Bîrzan et al. 2004; Dunn & Fabian 2004; McNamara & Nulsen 2007). Of the nine systems studied here with *XMM–Newton*, six have significant detections of cavities associated with the radio lobes [3C 296, NGC 1044, NGC 4261, 3C 66B (Croston et al. 2003), 3C 449 (Croston et al. 2003) and NGC 6251 (Evans et al. 2005)]. In several cases where a cavity is not identifiable in the X-ray data, the emission is nevertheless elongated perpendicular to the direction of the radio axis (3C 76.1, NGC 315), which suggests a link between the structure of the X-ray emitting gas and the radio source.

5.1.1 Correlations between X-ray and radio properties

While the images presented in the previous sections clearly indicate an important relationship between the radio and X-ray properties of these systems, the extent to which the environmental properties control the large-scale radio morphology remains difficult to establish observationally. We looked for correlations between the radio luminosity, radio-source projected physical size, axial ratio, internal pressure and the environmental properties as determined from our X-ray observations (X-ray luminosity, gas temperature, β, r_c, external pressure, ratio of external to internal pressure and pressure gradient at the radius of the lobes). Table 7 lists the results of Spearman rank tests for each pair of parameters. The strongest correlations are plotted in Fig. 8.

Table 7. Correlations between radio-source and group gas properties, determined using the Spearman rank test. Column 3 is the value of Student's *t* for the given comparison, and column 4 is the null hypothesis probability (NHP), i.e. the probability of obtaining the given value of Student's *t* from an uncorrelated data set.

Parameter 1	Parameter 2	t	NHP
L_R	L_X	0.088 241	0.466
	T_X	0.044 102	0.483
	β	1.396017	0.103
	r_c	0.683 130	0.258
	P_{ext}	0.883 277	0.203
	$P_{\mathrm{ext}}/P_{\mathrm{int}}$	0.447	0.334
	$\mathrm{d}P/\mathrm{d}r$	0.293 695	0.389
D	L_X	0.221 249	0.416
	T_X	0.883 277	0.203
	β	0.221 249	0.416
	r_c	1.272 136	0.12
	P_{ext}	2.853 810	0.012
	$P_{\mathrm{ext}}/P_{\mathrm{int}}$	2.263	0.029
	$\mathrm{d}P/\mathrm{d}r$	1.705 606	0.070
r_{ax}	L_X	0.634 866	0.273
	T_X	1.098 087	0.154
	β	1.098 087	0.154
	r_c	0.988 538	0.178
	P_{ext}	1.819 606	0.056
	$P_{\mathrm{ext}}/P_{\mathrm{int}}$	1.396	0.103
	$\mathrm{d}P/\mathrm{d}r$	1.506 237	0.0914
P_{int}	L_X	0.088 241	0.466
	T_X	0.781 661	0.23
	β	0.176 777	0.432
	r_c	0.935 414	0.190
	P_{ext}	3.743 997	0.0036
	$\mathrm{d}P/\mathrm{d}r$	1.326 473	0.113

We found that radio luminosity is uncorrelated with any of the group gas properties; however, some correlations were found between external pressure (measured at the midpoint of the source) and the projected radio-source size, axial ratio and external pressure. In particular, correlations that are significant at the ~90 per cent confidence level or higher were found between radio-source size (in kpc) and both external pressure and pressure gradient (null hypothesis probabilities of 1.2 and 7 per cent, respectively), and between axial ratio and both external pressure and pressure gradient (null hypothesis probabilities of 5.6 and 9.1 per cent, respectively). Although these results are not highly significant (and are somewhat dominated by the two largest sources, NGC 315 and NGC 6251: see Fig. 8), they suggest a link between radio-source evolution and group gas properties. However, the correlation of radio-source size with external pressure and pressure gradient may simply result from a selection effect: we might expect the largest sources to probe further out into the group atmospheres, where the pressure is lower and the gradient likely to be steeper. To test this explanation, we determined the external pressures at a fixed physical radius of 300 kpc (comparable to the projected distances probed by the lobes of NGC 315 and NGC 6251), which we consider to be an effective pressure normalization for the outer regions of each group. If the correlation between current source size and axial ratio with external pressure acting on the lobe is due solely to the fact that the larger sources can reach lower pressure regions of the groups, then we would expect no systematic difference in the pressure normalization at a fixed physical radius as a function of source size or axial ratio. Indeed, this is what we find, and so we conclude that the correlations with external pressure and its gradient are most likely to be a selection effect. The lack of correlations between radio-source structure and β and r_c support this explanation. As radio-source size and axial ratio are themselves strongly correlated (larger sources tend to have small axial ratios), it is plausible that the correlations with axial ratio have the same explanation; however, the size-axial ratio relationship itself is likely to be telling us something about FR I evolution, and so the different external pressures and pressure gradients experienced by the smaller, and typically fatter sources (high pressures and flatter-pressure gradients) compared to the larger, and typically thinner sources (low pressures and steeper-pressure gradients), may be a determining factor in evolving a large FR I source.

We also find significant correlations between both radio-source size and axial ratio and the pressure ratio, $P_{\mathrm{ext}}/P_{\mathrm{int}}$, with null hypothesis probabilities of 2.9 and 10 per cent, respectively. We will discuss the relationship between pressure ratio (which we consider to be a measure of the size of the energetic contribution required from non-radiating particles – see below) and radio-source structure in more detail in Section 5.2.

The lack of correlations between X-ray luminosity/temperature and any of the radio properties of these systems indicates that radio-source structure is independent of group environment properties. Our sample covers the full range of typical FR I radio morphologies, slightly more than an order of magnitude in radio luminosity, and as discussed in the previous section, nearly two orders of magnitude in X-ray luminosity. We can therefore conclude that, while all of the FR I radio sources in our sample have been found to inhabit group-scale environments, the evolution of their radio structure appears to be unrelated to the richness of the group environment, as parametrized by the X-ray luminosity and temperature. The only

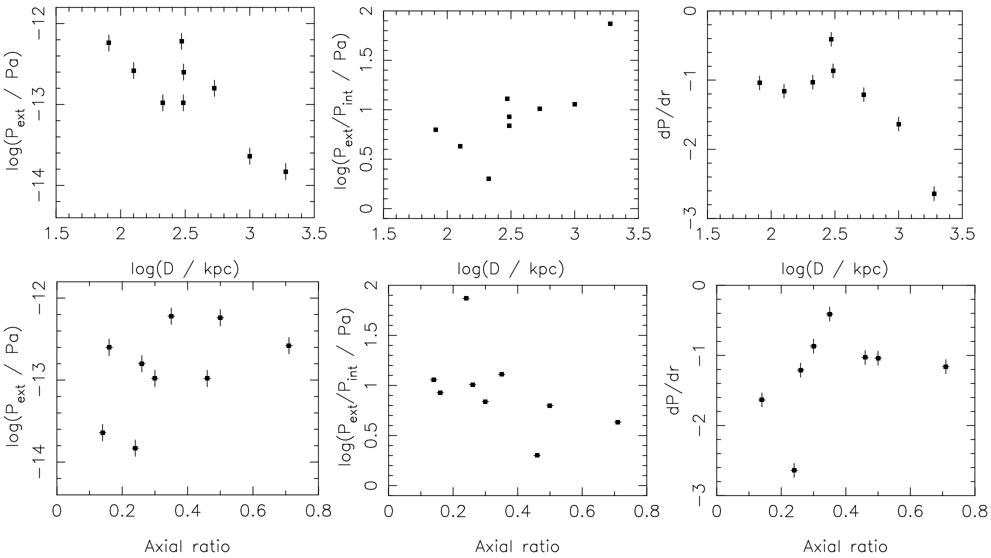

Figure 8. Correlations between radio structure and group gas properties. Top panel: size versus external pressure (left-hand panel), pressure ratio ($P_{\rm ext}/P_{\rm int}$) (middle panel) and pressure gradient (right-hand panel); bottom panel: axial ratio versus external pressure (left-hand panel), pressure ratio ($P_{\rm ext}/P_{\rm int}$) (middle panel) and pressure gradient (right-hand panel).

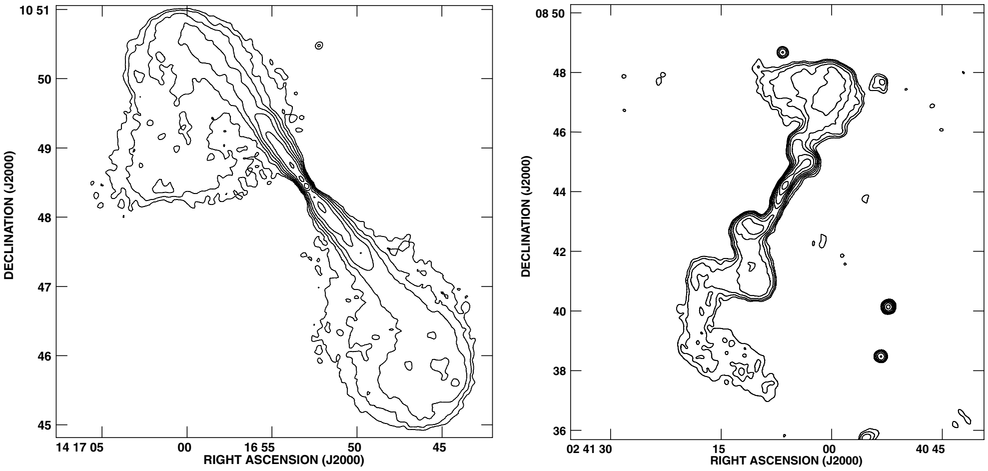

Figure 9. Examples of the two morphological classes of FR I radio galaxies, as described in the text. Left-hand panel: a typical 'bridged' source, 3C 296, in which the lobe material is primarily between the nucleus and the end of the collimated jet; Right-hand panel: a typical 'plumed' source, NGC 1044, in which the lobe material is primarily beyond the end of the collimated jet.

environmental properties that may be relevant to the source evolution are the group pressure and pressure distribution.

5.1.2 *Radio morphological class and environment*

To investigate the relationship between radio structure and environment further, we divide the radio sources based on their large-scale morphology into the two classes of 'plumed' and 'bridged' sources, as defined by Leahy, Bridle & Ström (1998).[3] By this definition, 'plumed' FR Is are those in which the majority of lobe material is beyond the end of the collimated jet, whereas in 'bridged' FR Is, the majority of lobe material is between the end of the collimated jet and the nucleus. Fig. 9 shows radio maps of a typical member of each class. Based on this definition, we classified NCG 1044, 3C 31, NGC 315, NGC 6251 and 3C 449 as 'plumed' sources, and 3C 296, 3C 76.1, 3C 66B and NGC 4261 as 'bridged' sources.

We first tested whether the jet power is the controlling parameter in determining whether a source shows a bridged or plumed morphology by comparing the 178-MHz radio luminosities of the two subsamples. We found no difference in the radio luminosity distributions of the two classes, and so we conclude that environment must play at least some role in determining the large-scale radio structure. We note that for this sample, the size distributions of the two classes are significantly different (Fig. 10), with plumed sources being typically larger than bridged sources. Results of Kolmogorov–Smirnov (KS) tests comparing the X-ray-measured group properties are shown in Table 8. We find no significant differences between the intrinsic group properties of the two subsamples, but do find a significant difference between the pressure ratios ($P_{\rm ext}/P_{\rm int}$) for the two subsamples, as discussed in Section 5.2.

---

[3] http://www.jb.man.ac.uk/atlas/anatomy.html

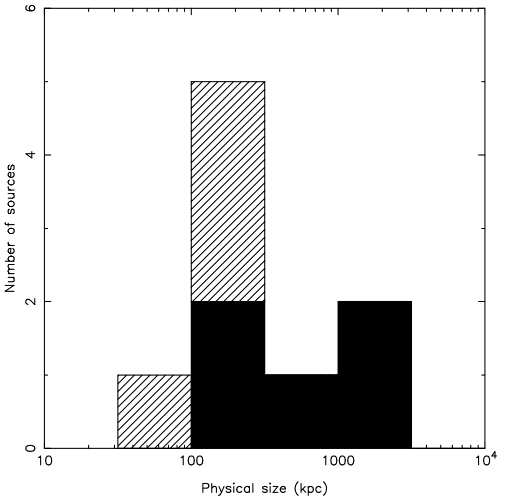

Figure 10. Histograms of radio-source size for the bridged (hatched) and plumed (solid black) sources, showing a statistically significant difference in their distributions.

We conclude that the current X-ray data do not conclusively demonstrate any close relationship between environmental conditions and radio-source structure. It appears that both plumed and bridged sources can be produced in a range of environments, although the difference in typical sizes (and axial ratios) of the two classes, together with the results discussed in the previous section, suggests that the two classes may represent an evolutionary sequence in which the environment plays some role in turning bridge structures into plumes. An evolutionary model of this sort would require a transition from one morphology to the other. A combination of buoyancy effects and collapse due to the end of overpressuring could produce such a transition (e.g. Hardcastle 1999); however, while sources exist in which one side is bridged and the other plumed (e.g. 3C 66B), objects in a state of transition between bridged and plumed structures do not appear to be common in the FR I population, which suggests that the time-scale for the transition would need to be short.

5.2 Source dynamics and particle content

Fig. 11 shows external pressure profiles for the eight sources observed with *XMM–Newton*, determined from the most probable pressure at each radius based on the MCMC probability distribution as discussed in the previous section, with internal, equipartition pressures overplotted. The plotted uncertainty range takes into account uncertainties in both the temperature and the surface-brightness model. Internal equipartition pressures were determined for each radio source, and for different components of the source where appropriate, using the code of Hardcastle, Birkinshaw & Worrall (1998a). The electron energy spectrum was normalized using flux densities measured from the 1.4-GHz maps of Table 2 with 178-MHz flux densities from the 3CRR catalogue (Laing, Riley & Longair 1983) included where available. We assumed $\gamma_{\min} = 10$, $\gamma_{\max} = 10^6$, an energy injection index of $\delta = 2$ (corresponding to radio spectral index $\alpha = 0.5$) with a break in the spectrum in the region of $\gamma = 5 \times 10^3$–5×10^4 as appropriate to fit the radio data points. The equipartition pressures assume no contribution from protons.

5.2.1 *Particle content and radio morphology*

In agreement with previous studies using earlier X-ray observatories (e.g. Morganti et al. 1988; Worrall & Birkinshaw 2000) and using *XMM–Newton* (e.g. Croston et al. 2003), we found that the measured external pressures from the hot-gas environments were in many cases significantly higher than the minimum internal pressures for the radio lobes (if it is assumed that the sources are in the plane of the sky; relaxation of this assumption does not affect our conclusions, as discussed below). Fig. 12 (top panel) shows histograms of the pressure ratios ($P_{\rm ext}/P_{\rm int}$) for the 16 lobes in the sample (only one lobe is within the *XMM–Newton* field of view for NGC 315 and NGC 6251) showing that the lobes range from being apparently underpressured by a factor of ~70 to approximate pressure balance.

This is the first time that such a study has been carried out for a sample that includes a wide range of observed FR I radio morphologies, and so a primary aim of our work was to investigate whether the amount of 'missing' pressure is related to the properties of the radio-source and/or its environmental interaction. If we consider two extreme cases, 3C 296, which are apparently slightly overpressured, and 3C 449, which are apparently underpressured by a factor of 10, it is clear that 3C 296 is a typical bridged source, whereas 3C 449 is plumed. This morphological difference, together with the correlations between radio-source structure and pressure ratio noted in the previous section, suggests a model in which jet/environment interactions affect the particle and/or energy content of the radio lobes; for example, the dominant factor in determining the ratio of radiating to non-radiating particles may be the efficiency of the entrainment process. We would expect that the entrainment rate for plumed sources is higher, as a larger fraction of the jet surface is in direct contact with the external medium, whereas a jet that is embedded in a lobe is not in direct contact with the group gas (except perhaps very close to the nucleus), and so its entrainment rate might be expected to be lower. If the amount of entrained material is sufficient to affect significantly the internal energy density of the radio lobes (which is likely to require heating of the entrained matter), then we might expect to see a larger apparent imbalance in the plumed sources.

The lower panel of Fig. 12 shows histograms of the pressure ratios for the two categories, which demonstrate that there is indeed a significant difference in the two populations in the expected sense: the bridged sources are typically closer to pressure balance at equipartition than the plumed sources. Using a KS test, we can exclude the hypothesis that the two subsamples are drawn from the same parent population at a confidence level of >97 per cent. As shown in Table 8, this does not appear to be solely due to differences in the internal pressures for the two subsamples. We note that the most extreme pressure ratio in the 'bridged' category is the eastern lobe of 3C 66B, which has a ratio of 11.5. The classification of this source as bridged is ambiguous, because the eastern jet does not enter the lobe for some distance from the nucleus (see e.g. Hardcastle et al. 1996). All of the other bridged lobes have ratios <5, and so the distinction between the two populations is considerably more significant if the eastern lobe of 3C 66B is excluded (a single parent population can be excluded at the 99.8 per cent confidence level).

This comparison therefore supports the hypothesis that entrainment of the jet's surroundings on scales of tens to hundreds of kpc is responsible for the apparent pressure imbalance of FR I radio galaxies. Unfortunately, there is no obvious observational proxy for jet deceleration or entrainment that can be used to test this hypothesis further with the current data. However, comparisons with the models of Laing & Bridle (2002b, and in preparation) show that plumed

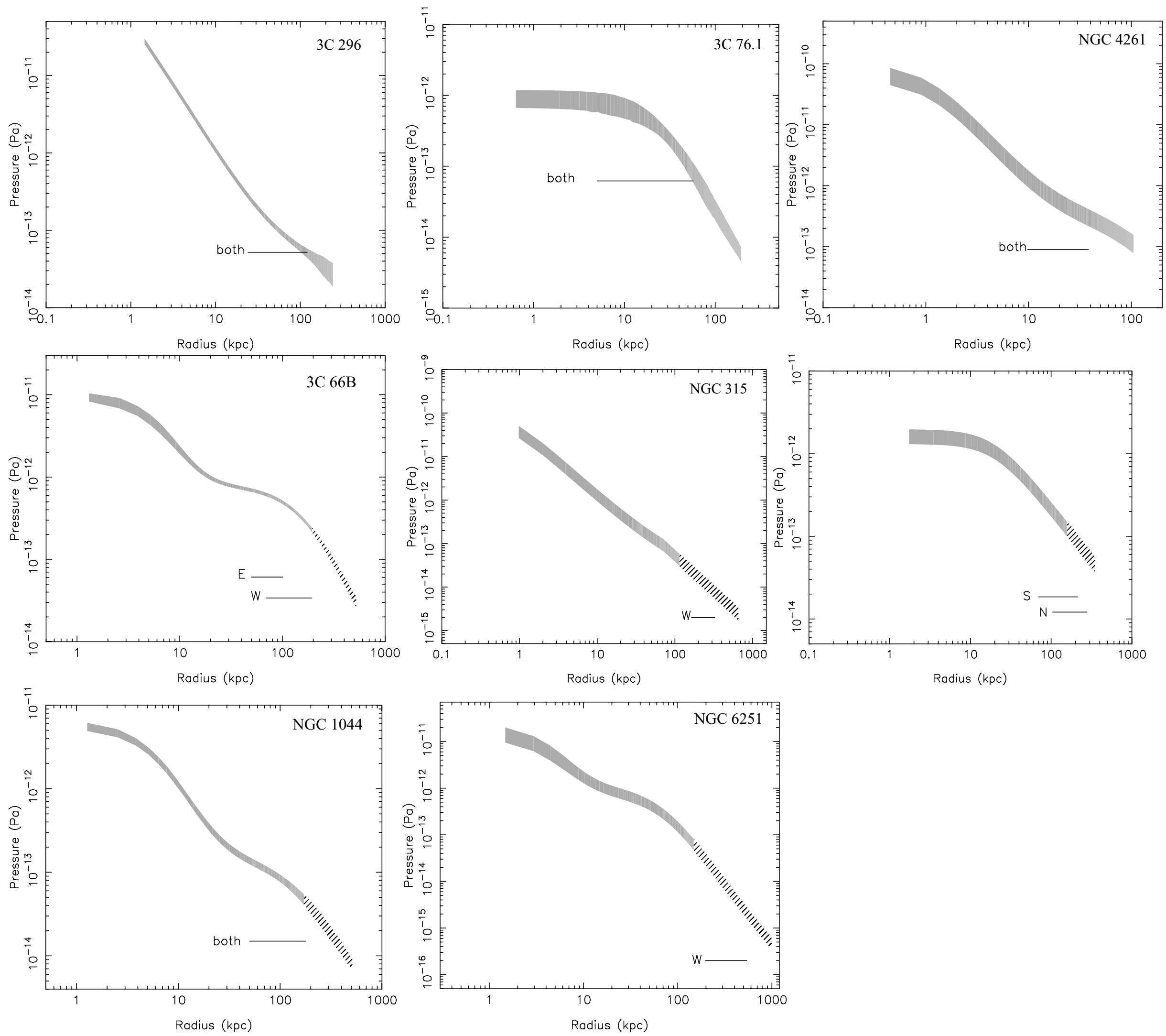

Figure 11. Pressure profiles for the *XMM*-observed radio-galaxy environments. The grey-shaded area indicates the 1σ uncertainty, which takes into account uncertainties in all the model parameters and in the temperature measurement. Hatched regions indicate an extrapolation of the pressure profile model beyond the region covered by the data. Horizontal lines indicate internal pressures of radio lobes. Top row (left to right-hand side): the bridged sources 3C 296, 3C 76.1, NGC 4261; middle row: the plumed sources 3C 66B, NGC 315 and 3C 449; bottom row: NGC 1044 and NGC 6251 (also plumed).

sources such as 3C 31 have an entrainment rate that increases with distance from the nucleus, whereas bridged sources such as 3C 296 may not. Clearly, the entrainment characteristics of jets that are directly in contact with the external medium will be different from those of jets that propagate inside lobe material. The strong correlation between pressure ratio and axial ratio discussed in the previous section also provides support for this model.

5.2.2 *Projection effects*

The pressure comparisons discussed here use projected distances, and hence the true pressure ratios are likely to be somewhat different. For a radio source at a small angle to the line of sight, the source volume will have been underestimated, leading to an overestimate of $P_{\rm int}$. At the same time, the external pressure acting at the midpoint and outer edge of the lobe ($P_{\rm ext}$) will be overestimated, because the radio source will extend further out into the atmosphere which is decreasing in pressure with radius. Hence, the extent to which the pressure ratio is affected depends on the particular system. In Croston et al. (2003), we argued that for 3C 449 an angle of $<11^\circ$ to the line of sight would be required to obtain pressure balance, whereas the two-sided nature of its jets imply $\theta > 75^\circ$ (Feretti et al. 1999). For $\theta = 75^\circ$, the pressure ratio decreases by only 3 per cent from that obtained for the assumption that the source is in the plane of the sky (from 12.0 to 11.6 for the northern plume). It is clear that projection alone cannot be responsible for the large apparent pressure imbalance in this plumed source. The source likely to be most affected by projection effects is NGC 6251, which has a one-sided jet on large scales. Jones et al. (2002) argue that $\theta < 40^\circ$, based on pc-scale sidedness limits. We find that an angle of $<12^\circ$ is required for the pressure ratio at the midpoint of the western plume of NGC 6251 to be consistent with the median value for the bridged sources ($P_{\rm ext}/P_{\rm int} = 3.3$). Such a small angle cannot be ruled out, but given the large projected size of this source, it is implausible

Table 8. Comparison of environmental properties for bridged and plumed sources. Column 2 gives the KS D value for a comparison between the bridged and plumed subsamples and column 3 gives the null hypothesis probability for the subsamples being drawn from the same parent population. For the pressure ratio comparison, each radio lobe was treated separately, whereas the other comparisons are for the source as a whole. $E_{\rm ratio}$ is the ratio between $E_{\rm req}$ and $E_{\rm rg}$ (see Table 6).

Parameter	D	NHP
$L_{\rm X}$	0.50	0.37
$T_{\rm X}$	0.40	0.65
β	0.50	0.37
r_c	0.60	0.18
$P_{\rm ext}$	0.47	0.45
$P_{\rm ext}/P_{\rm int}$	0.78	0.005
$P_{\rm int}$	0.67	0.10
$\mathrm{d}P/\mathrm{d}r$	0.50	0.37
$E_{\rm req}$	0.60	0.26
$E_{\rm rg}$	0.43	0.55
$E_{\rm ratio}$	0.60	0.26

(an angle of $<12°$ over the entire length of the source leads to a physical size >10 Mpc – see e.g. Birkinshaw & Worrall 1993). An angle of $\sim 40°$, consistent with the pc-scale constraints, would give a more modest reduction in pressure ratio, resulting in $P_{\rm ext}/P_{\rm int} \sim 29$. In addition, estimates for the line-of-sight angles for other plumed sources (3C 31 and NGC 315) from kinematic modelling of the radio data are not extreme (Laing & Bridle 2002a; Laing et al. 2006). We conclude that the difference between the apparent pressure imbalances of bridged and plumed sources is not solely the result of projection effects.

5.2.3 *Implications*

If the model we propose here to explain the apparent pressure deficit is correct for this sample of FR Is, then an obvious question is whether it is consistent with the pressure offsets observed in cluster-centre radio sources (e.g. Morganti et al. 1988; Bîrzan et al. 2004; Dunn & Fabian 2004), which typically do not possess well-collimated jets on large scales. Given the amorphous structures of many cluster-centre sources, suggestive of strong environmental influence, it seems plausible that there is considerable mixing of cluster gas with radio-lobe plasma (and heating, as required in order for the cavities to be detected) before the bubbles rise in the cluster atmosphere. In addition, Dunn, Fabian & Celotti (2006) argue that even in bubbles with large apparent pressure offsets such as those of the Perseus cluster, the jet is initially leptonic, so that the pressure offset on large scales is more likely to be due to entrainment rather than a relativistic proton population, consistent with the picture we present here. Hence, while the categorization of group-scale sources into bridged and plumed morphologies with different energetics may not be directly applicable to cluster-centre sources, these results may nevertheless provide some insight into the solution of the pressure balance problem for these systems as well.

An alternative model could be proposed in which the strength of the interaction dictates the level of entrainment. For example, sources that are overpressured may be less easily disrupted, so that entrainment levels are low, while sources close to pressure balance are more susceptible to turbulence and higher entrainment rates. It is unclear how such a picture would work in detail; however, our data do not allow us to rule out such a model.

5.3 Environmental impact

As discussed in Section 5.1, it is clear that the group gas surrounding FR I radio galaxies is strongly affected by their presence. Earlier *XMM–Newton* studies of the group environments of FR Is found direct evidence for localized heating of the group gas, and indirect evidence for more generalized heating (Croston et al. 2003). In Croston et al. (2005a), we reported an apparent systematic difference in the radio properties of galaxy groups with and without central radio sources, in the sense that radio-loud groups appear to be systematically hotter for a given luminosity. A recent study comparing REFLEX/NORAS clusters with NVSS has found similar results (Magliocchetti & Brüggen 2007), while a *Chandra* study of a subset of the Croston et al. (2005a) sample by Jetha et al. (2007) has shown that the gas properties in the innermost regions of the group do not appear to be significantly affected by the presence of a

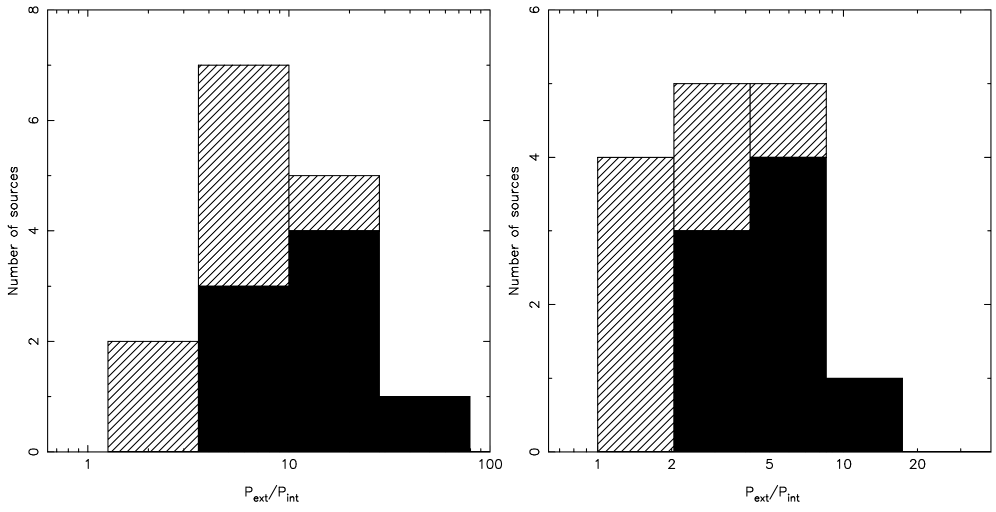

Figure 12. Histograms of $P_{\rm ext}/P_{\rm int}$, the ratio of external to internal (equipartition) pressure for the full sample. The left-hand panel is for pressures at the midpoint of the radio lobe and the right-hand panel for pressures at the outermost of edge of the radio lobe. The sample is subdivided into bridged (hatched) and plumed (solid black) lobes. For all except NGC 6251 and NGC 315, both lobes are plotted.

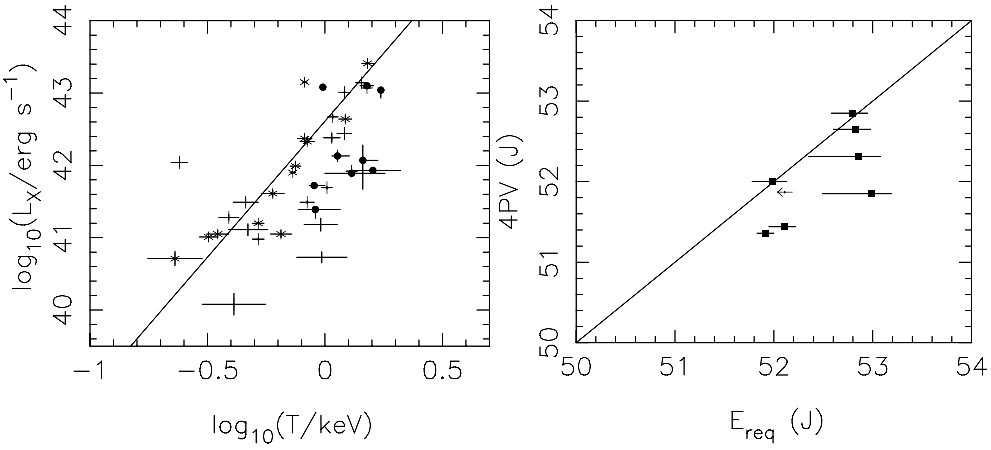

Figure 13. Left-hand panel: The L_X–T_X relation for the *XMM–Newton* radio-galaxy environments sample (filled circles) compared with the radio-quiet samples (*x* symbols) and radio-loud (+ symbols) samples of Croston et al. (2005a). The solid line indicates the best-fitting relation for radio-quiet groups. Right-hand panel: the energy required to produce the observed temperature offsets ($C\ \Delta\ T$) versus energy available from the current radio source ($4PV$). The solid line represents equality of the two energies.

radio source, so that any heating processes must be most significant on larger scales, comparable to the size of the radio lobes.

In Fig. 13, we show the X-ray luminosity–temperature relation for the current sample of nine radio-galaxy group environments (filled circles). The × and + symbols indicate the radio-quiet and radio-loud samples of Croston et al. (2005a), respectively, and the solid line indicates the best-fitting relation for the radio-quiet groups. The points for the *XMM–Newton* radio-galaxy sample all lie to the high-temperature side of the radio-quiet relation, thus confirming the earlier result: groups containing extended radio sources scatter to higher temperatures for a given X-ray luminosity. In Croston et al. (2005a), we argued, based on a lack of difference in the X-ray-to-optical luminosity ratios for the two subsamples, that this effect must be due to a temperature increase, rather than the expected luminosity decrease. The origin of this effect therefore remains unclear. It would be expected that any energy injected into the environment would alter both its luminosity and temperature, with proportionate increases in both if the gas remains in hydrostatic equilibrium. This is consistent with the position of the FR I groups on the L_X–T_X diagram. It has been argued that the slope of the L_X–T_X relation is set mainly by the effects of radiative cooling (Voigt & Fabian 2004); the offset associated with radio-loud AGN activity that we observe here may therefore have the primary effect of increasing the scatter in the L_X–T_X relation, rather than altering its slope.

We checked whether it was possible that the presence of extended non-thermal emission in the radio-galaxy environments could be biasing our temperature estimates by fitting a combined *mekal* plus power-law model to the groups with the largest temperature excesses, NGC 1044 and NGC 4261, with the temperature fixed at that predicted by the radio-quiet L_X–T_X relation. In both the cases, acceptable fits with power-law indices between 1.6 and 2 were obtained. In the case of NGC 4261, the fit statistic was considerably worse for this model ($\chi^2 = 1124$ for 626 d.o.f.), whereas for NGC 1044 the fit statistic was very similar to that of the *mekal*-only model ($\chi^2 = 160$ for 129 d.o.f.). The X-ray luminosities of the non-thermal components were $\sim 6 \times 10^{41}$ erg s^{-1} in both cases, comparable to the total luminosity of the group. We cannot, therefore, rule out the presence of extended non-thermal X-ray emission in all of the groups in the sample from spectral data alone. To explain the entire 'temperature excess' in this way would, however, require a large fraction of the measured X-ray luminosity to originate in extended non-thermal emission.

Column 14 of Table 6 lists the energy required to raise the temperature of all the group gas within the spherical region enclosing the radio galaxy by ΔT, the difference between the observed gas temperature in that region and the temperature predicted for a group of the same luminosity using the radio-quiet L_X–T_X relation of Croston et al. (2005a). To try to understand whether the radio source is capable of producing these effects, we estimated the total energy available from the current episode of radio activity as $4PV$ (this includes the energy stored in the lobes, which cannot yet have had an effect on the environment), using the total lobe volume and the pressure at the lobe midpoint. Fig. 13 (right-hand panel) compares the required and available energies for each source. As shown in Table 8, there is no significant difference in the ratios of required to available energy for the bridged and plumed sources. In five of the eight sources with temperature excesses, the radio source appears to be sufficiently powerful to heat the gas by the required amount, but in three cases (3C 31, NGC 4261 and NGC 315) the available energy is significantly less than that required. It has been argued previously (e.g. Nipoti & Binney 2006) that if AGN radio outbursts are an intermittent process, then it is most probable that we will observe outbursts whose energy injection rate is lower than the average for the system. However, if the higher than expected temperatures in these systems are the result of radio-source energy injection, then they would be expected to disappear on time-scales comparable to the sound crossing time, so it is not clear that previous outbursts from these AGN can be responsible for the effect we observe. Another possibility, which is difficult to rule out, is that radio-loud AGN prefer to inhabit hotter than average group environments.

6 CONCLUSIONS

We have carried out the first *XMM–Newton* study of a sample of low-power (FR I) radio galaxies and their environments. We find the following results.

(i) The radio galaxies inhabit group-scale hot-gas environments with luminosities ranging from 2×10^{41} erg s^{-1} to 10^{43} erg s^{-1}, consistent with earlier studies of FR I environments.

(ii) The radio properties of the FR Is, including radio luminosity, source size and axial ratio, are uncorrelated with the richness of the group environments, as parametrized by either X-ray luminosity or temperature.

(iii) Marginally significant correlations were found between source size and external pressure and pressure gradient, and between axial ratio and both external pressure and pressure gradient, with long, narrow sources associated with lower pressures and steeper gradients; however, this could simply be a selection effect, as longer sources (which tend to be narrower) are able to probe the outer regions of groups, where the pressure gradient is steeper.

(iv) In agreement with earlier work, we find that FR I radio galaxies are acted on by external pressures that are significantly higher than their internal, equipartition pressures, with apparent pressure imbalances ranging from a factor of 70 times underpressured to rough pressure balance.

(v) We report for the first time that the apparent pressure imbalance is linked to radio-source morphology: 'plumed' FR I sources typically have large pressure deficits, whereas 'bridged' FR Is are closer to pressure balance. We interpret this result as evidence that 'plumed' sources have a higher ratio of non-radiating to radiating particles than 'bridged' sources, which is likely to be caused by the higher entrainment rate expected for 'plumed' sources.

(vi) We find that the temperatures of the FR I group environments are typically significantly higher than predicted for their luminosity, which supports our earlier claim for a temperature excess in radio-loud groups. In 5/8 sources, the current radio source may be sufficiently powerful to have produced this excess via heating; however, in three cases the current source is too weak. We conclude that radio-source heating remains the most plausible explanation for this result; however, we cannot rule out an alternative explanation in which hotter groups are more favourable for the generation of an FR I radio source.

ACKNOWLEDGMENTS

We thank Etienne Pointecouteau, Monique Arnaud and Gabriel Pratt for developing the background-subtraction method used in this paper, for providing filter-wheel closed background data sets and for useful discussions about *XMM–Newton* background subtraction. We also thank the referee for helpful comments. MJH thanks the Royal Society for a Research Fellowship. This work is partly based on observations obtained with *XMM–Newton*, an ESA science mission with instruments and contributions directly funded by ESA Member States and the USA (NASA). The National Radio Astronomy Observatory is a facility of the National Science Foundation operated under cooperative agreement by Associated Universities, Inc.

REFERENCES

Arnaud M., Pointecouteau E., Pratt G. W., 2005, A&A, 441, 893
Basson J. F., Alexander P., 2003, MNRAS, 339, 353
Belsole E., Worrall D. M., Hardcastle M. J., Birkinshaw M., Lawrence C. R., 2004, MNRAS, 352, 924
Bicknell G. V., 1994, ApJ, 422, 542
Birkinshaw M., Worrall D. M., 1993, ApJ, 412, 568
Bîrzan L., Rafferty D. A., McNamara B. R., Wise M. W., Nulsen P. E. J., 2004, ApJ, 607, 800
Blanton E. L., Sarazin C. L., McNamara B. R., Wise M. W., 2001, ApJ, 558, L15
Böhringer H., Voges W., Fabian A. C., Edge A. C., Neumann D. M., 1993, MNRAS, 264, L25
Böhringer H. et al., 2007, A&A, 469, 363
Bower R. G., Benson A. J., Malbon R., Helly J. C., Frenk C. S., Baugh C. M., Cole S., Lacey C. G., 2006, MNRAS, 370, 645
Brüggen M., Kaiser C. R., 2001, MNRAS, 325, 676
Croston J. H., Hardcastle M. J., Birkinshaw M., Worrall D. M., 2003, MNRAS, 346, 1041
Croston J. H., Birkinshaw M., Hardcastle M. J., Worrall D. M., 2004, MNRAS, 353, 879
Croston J. H., Hardcastle M. J., Birkinshaw M., 2005a, MNRAS, 357, 279
Croston J. H., Hardcastle M. J., Harris D. E., Belsole E., Birkinshaw M., Worrall D. M., 2005b, ApJ, 626, 733
Croton D. J. et al., 2006, MNRAS, 365, 11
Croston J. H., Kraft R. P., Hardcastle M. J., 2007, ApJ, 660, 191
Dunn R. J. H., Fabian A. C., 2004, MNRAS, 355, 862
Dunn R. J. H., Fabian A. C., Taylor G. B., 2005, MNRAS, 364, 1343
Dunn R. J. H., Fabian A. C., Celotti A., 2006, MNRAS, 372, 1741
Evans D. A., Hardcastle M. J., Croston J. H., Worrall D. M., Birkinshaw M., 2005, MNRAS, 359, 363
Evans D. A., Worrall D. M., Hardcastle M. J., Kraft R. P., Birkinshaw M., 2006, ApJ, 642, 96
Fabian A. C., Sanders J. S., Allen S. W., Crawford C. S., Iwasawa K., Johnstone R. M., Schmidt R. W., Taylor G. B., 2003, MNRAS, 344, L43
Fanaroff B. L., Riley J. M., 1974, MNRAS, 167, 31
Feretti L., Perley R., Giovannini G., Andernach H., 1999, A&A, 341, 29
Forman W. et al., 2007, ApJ, 665, 1057
Gliozzi M., Sambruna R. M., Brandt W. N., 2003, A&A, 408, 949
Gregory P. C., 2005, Bayesian Logical Data Analysis for the Physical Sciences: A Comparative Approach with 'Mathematica' Support. Cambridge Univ. Press, Cambridge
Hardcastle M. J., 1999, A&A, 349, 381
Hardcastle M. J., Alexander P., Pooley G. G., Riley J. M., 1996, MNRAS, 278, 273
Hardcastle M. J., Birkinshaw M., Worrall D. M., 1998a, MNRAS, 294, 615
Hardcastle M. J., Worrall D. M., Birkinshaw M., 1998b, MNRAS, 296, 1098
Hardcastle M. J., Worrall D. M., Birkinshaw M., Laing R. A., Bridle A. H., 2002, MNRAS, 334, 182
Hardcastle M. J., Worrall D. M., Birkinshaw M., Laing R. A., Bridle A. H., 2005, MNRAS, 358, 843
Hardcastle M. J., Evans D. A., Croston J. H., 2006, MNRAS, 370, 1893
Hobson M. P., Baldwin J. E., 2004, Appl. Opt., 43, 2651
Jetha N. N., Ponman T. J., Hardcastle M. J., Croston J. H., 2007, MNRAS, 376, 193
Jones C., Forman W., Vikhlinin A., Markevitch M., David L., Warmflash A., Murray S., Nulsen P. E. J., 2002, ApJ, 567, L115
Kataoka J., Stawarz Ł., 2005, ApJ, 622, 797
Kim D.-W., Fabbiano G., 2004, ApJ, 611, 846
Komossa S., Böhringer H., 1999, A&A, 344, 755
Kraft R. P., Vázquez S. E., Forman W. R., Jones C., Murray S. S., Hardcastle M. J., Worrall D. M., Churazov E., 2003, ApJ, 592, 129
Laing R. A., 1993, in Burgarella D. et al., eds, Astrophysical Jets. Cambridge University Press, Cambridge, p. 95
Laing R. A., Bridle A. H., 2002a, MNRAS, 336, 328
Laing R. A., Bridle A. H., 2002b, MNRAS, 336, 1161
Laing R. A., Riley J. M., Longair M. S., 1983, MNRAS, 204, 151
Laing R. A., Canvin J. R., Cotton W. D., Bridle A. H., 2006, MNRAS, 368, 48
Laing R. A., Bridle A. H., Parma P., Feretti L., Giovannini G., Murgia M., Perley R. A., 2008, MNRAS, in press (doi:10.1111/j.1365-2966.2008.13091.x)
Leahy J. P., Bridle A. H., Ström R. G., 1998, An Atlas of DRAGNs (http://www.jb.man.ac.uk/atlas)
Lumb D. H., Warwick R. S., Page M., De Luca A., 2002, A&A, 389, 93
McNamara B. R., Nulsen P. E. J., 2007, ARA&A, 45, 117
Magliocchetti M., Brüggen M., 2007, MNRAS, 379, 260
Morganti R., Fanti R., Gioia I. M., Harris D. E., Parma P., de Ruiter H., 1988, A&A, 189, 11
Nipoti C., Binney J., 2005, MNRAS, 361, 428
Osmond J. P. F., Ponman T. J., 2004, MNRAS, 350, 1511

Read A. M., Ponman T. J., 2003, A&A, 409, 395
Reynolds C. S., Heinz S., Begelman M. C., 2002, MNRAS, 332, 271
Sambruna R. M., Gliozzi M., Eracleous M., Brandt W. N., Mushotzky R., 2003, ApJ, 586, L37
Voigt L. M., Fabian A. C., 2004, MNRAS, 347, 1130
Worrall D. M., Birkinshaw M., 1994, ApJ, 427, 134
Worrall D. M., Birkinshaw M., 2000, ApJ, 530, 719
Worrall D. M., Birkinshaw M., Laing R. A., Cotton W. D., Bridle A. H., 2007, MNRAS, 380, 2
Zezas A., Birkinshaw M., Worrall D. M., Peters A., Fabbiano G., 2005, ApJ, 627, 711

This paper has been typeset from a TEX/LATEX file prepared by the author.